

PULMONARY LESION CLASSIFICATION USING CONVOLUTIONAL NEURAL NETWORK FOR
ENDBRONCHIAL ULTRASONOGRAM



A Dissertation Submitted in Partial Fulfillment of the Requirements
for the Degree of Doctor of Philosophy in Computer Science and Information Technology
Department of Mathematics and Computer Science
FACULTY OF SCIENCE
Chulalongkorn University
Academic Year 2021
Copyright of Chulalongkorn University

การจำแนกรอยโรคปอดโดยใช้โครงข่ายประสาทสังวัตนาการสำหรับภาพเอ็นโดบรอนเคียลที่บันทึกด้วย
คลื่นเสียงความถี่สูง



วิทยานิพนธ์นี้เป็นส่วนหนึ่งของการศึกษาตามหลักสูตรปริญญาวิทยาศาสตรดุษฎีบัณฑิต
สาขาวิชาวิทยาการคอมพิวเตอร์และเทคโนโลยีสารสนเทศ ภาควิชาคณิตศาสตร์และวิทยาการ

คอมพิวเตอร์

คณะวิทยาศาสตร์ จุฬาลงกรณ์มหาวิทยาลัย

ปีการศึกษา 2564

ลิขสิทธิ์ของจุฬาลงกรณ์มหาวิทยาลัย

Thesis Title	PULMONARY LESION CLASSIFICATION USING CONVOLUTIONAL NEURAL NETWORK FOR ENDOBONCHIAL ULTRASONOGRAM
By	Miss Banphatree Khomkham
Field of Study	Computer Science and Information Technology
Thesis Advisor	Associate Professor RAJALIDA LIPIKORN, Ph.D.

Accepted by the FACULTY OF SCIENCE, Chulalongkorn University in
Partial Fulfillment of the Requirement for the Doctor of Philosophy

..... Dean of the FACULTY OF SCIENCE
(Professor POLKIT SANGVANICH, Ph.D.)

DISSERTATION COMMITTEE

..... Chairman
(Professor Kosin Chamnongthai, Ph.D.)

..... Thesis Advisor
(Associate Professor RAJALIDA LIPIKORN, Ph.D.)

..... Examiner
(Associate Professor NAGUL COOHAROJANANONE,
Ph.D.)

..... Examiner
(Associate Professor THANARAT CHALIDABHONGSE,
Ph.D.)

..... External Examiner
(Prem Junsawang, Ph.D.)

6173103823 : MAJOR COMPUTER SCIENCE AND INFORMATION TECHNOLOGY

KEYWORD: pulmonary lesion, endobronchial ultrasonography images (EBUS), convolutional neural network (CNN), radiomics features, gray-level co-occurrence matrix (GLCM), weighted ensemble

Banphatree Khomkham : PULMONARY LESION CLASSIFICATION USING CONVOLUTIONAL NEURAL NETWORK FOR ENDOBRONCHIAL ULTRASONOGRAM. Advisor: Assoc. Prof. RAJALIDA LIPIKORN, Ph.D.

This dissertation aims to develop a method to help classify pulmonary lesions from endobronchial ultrasonography images by proposing new features that are extracted from an EBUS image based on medical knowledge and a pulmonary lesion classification framework. The proposed features, namely the adaptive weighted-sum of the upper triangular gray-level co-occurrence matrix and the adaptive weighted-sum of the lower triangular gray-level co-occurrence matrix are used to determine heterogeneity, which is one of the most important characteristics of malignancy. The proposed features together with other standard features are used as input data for the proposed classification framework that uses the weighted ensemble classification based on the efficacy of the other three classification models. The first model uses random forest to classify a lesion based on the combination of radiomics features, the proposed features, and the patient's data. The second model uses EBUS images as input data to the tuned DenseNet 169 to classify a lesion. The third model uses multi-patch EBUS images as input data to the convolutional neural network to classify a lesion. The classification by the weighting ensemble function can improve the performance of the framework by combining the distinctive characteristics of each model. The data consists of 200 EBUS images from 200 patients: 124 malignant and 76 benign. From the experiment, it was found that the proposed framework yields 95% accuracy, 100% sensitivity, and 86.67% specificity.

Field of Study: Computer Science and Information Technology Student's Signature

Academic Year: 2021 Advisor's Signature

ACKNOWLEDGEMENTS

I would like to express my very great appreciation to my thesis advisor Associate Professor Dr. Rajalida Lipikorn for her valuable suggestions, continuous support, and generous supervision throughout my Ph.D. study.

I would like to thank Professor Dr. Kosin Chamnongthai, the chairman, Associate Professor Dr. Nagul Cooharajanone, Associate Professor Dr. Thanarat Chalidabhongse, and Dr. Prem Junsawang, the committee members for their valuable suggestions and comments on this dissertation.

I would like to thank Col. Anan Wattanathum, MD., and Jutamas Dechsanga, MD. From Pulmonary and Critical Care Division, Department of Medicine, Phramongkutklao Hospital for clinical advice and research data.

I would like to thank all the teachers who gave me all the knowledge. Moreover, I would like to thank my friends in the MIMIT lab, AMCS program, and CS program for giving suggestions about programming.

Additionally, I would like to thank the Development and Promotion of Science and Technology Talents Project (DPST) for financial aid.

Finally, I would also like to thank my family for their encouragement and support throughout my life.

จุฬาลงกรณ์มหาวิทยาลัย
CHULALONGKORN UNIVERSITY

Banphatree Khomkham

TABLE OF CONTENTS

	Page
ABSTRACT (THAI).....	iii
ABSTRACT (ENGLISH).....	iv
ACKNOWLEDGEMENTS.....	v
TABLE OF CONTENTS	vi
LIST OF TABLES.....	ix
LIST OF FIGURES	x
CHAPTER 1 INTRODUCTION	1
1.1 Statement of The Problem	1
1.2 Objectives	2
1.3 Scopes of Study	2
1.4 Contributions.....	3
1.5 Organization of The Dissertation.....	3
1.6 The Connection between Articles.....	4
1.7 Expected Outcomes.....	4
CHAPTER 2 PULMONARY LESION CLASSIFICATION FRAMEWORK.....	5
CHAPTER 3 PULMONARY LESION CLASSIFICATION FROM ENDOBRONCHIAL ULTRASONOGRAPHY IMAGES USING ADAPTIVE WEIGHTED-SUM OF THE UPPER AND LOWER TRIANGULAR GRAY-LEVEL CO-OCCURRENCE MATRIX.....	9
3.1 Introduction.....	10
3.2 Materials	14
3.3 Methods	15
3.3.1 Preprocessing	16
3.3.2 Window of Interest Selection	17
3.3.3 Feature Extraction	18

3.3.4 Feature Selection.....	21
3.3.5 Lesion Classification	24
3.3.6 Performance Evaluation.....	25
3.4 Experimental Results	26
3.5 Conclusions	29
CHAPTER 4 PULMONARY LESION CLASSIFICATION FRAMEWORK USING THE WEIGHTED ENSEMBLE CLASSIFICATION WITH RANDOM FOREST AND CNN MODELS FOR EBUS IMAGES.....	
4.1 Introduction.....	39
4.2 Materials	43
4.3 Methods	44
4.3.1 Preprocessing	45
4.3.1.1 Class Balancing.....	46
4.3.1.2 Mask Generation	47
4.3.1.3 Feature Extraction	48
4.3.1.4 WOI Selection	50
4.3.2 The Proposed Framework	50
4.3.2.1 Radiomics Feature and Patient Data-Based Model	50
4.3.2.2 Single Image-Based Model	51
4.3.2.3 Multi-Patch-Based Model	52
4.3.3 Weighted Ensemble Classification.....	56
4.3.4 Performance Evaluation.....	56
4.4 Experimental Results and Discussion	57
4.4.1 Experimental Setup.....	57
4.4.2 Experimental Results	57
4.4.2.1 EBUS Image Enhancement.....	57
4.4.2.2 Feature Selection	58

4.4.2.3 Classification Performance	59
4.5 Conclusions	66
CHAPTER 5 DISCUSSIONS AND CONCLUSIONS	72
5.1 Discussions and Conclusions.....	72
5.2 Limitations of Work	76
5.3 Suggestions and Future Works.....	77
APPENDIX.....	78
REFERENCES	83
VITA.....	85



LIST OF TABLES

	Page
Table 2.1 The difference between Article 1 and Article 2.....	8
Table 3.1 Features that are used for lesion classification.....	22
Table 3.2 Genetic algorithm parameters.....	24
Table 3.3 Classification results obtained from four classifiers with GA using 22 features.....	27
Table 3.4 Classification results obtained from four classifiers with GA using standard features + AWS and standard features + AWSU+AWSL.....	28
Table 3.5 Classification results obtained from four classifiers with GA using 34 features.....	28
Table 3.6 The selected features from P5 for SVM classifier.....	28
Table 3.7 Confusion matrix of using GA and SVM with features from P5.....	29
Table 3.8 Comparison of accuracy obtained from different gamma values.....	29
Table 4.1 Clinical details of the patients.....	44
Table 4.2 Distribution of EBUS images after class balancing.....	47
Table 4.3 The hyper-parameters of DenseNet 169 architecture.....	52
Table 4.4 The configuration of CNN for the multi-patch-based model.....	54
Table 4.5 The hyper-parameters of CNN architecture for the multi-patch-based model.....	54
Table 4.6 The classification performance of different classification models.....	60
Table 5.1 Distribution of test EBUS image data after applying augmentation.....	74
Table 5.2 The classification performance of different classification models.....	75

LIST OF FIGURES

	Page
Figure 2.1 Sample of an EBUS image.	7
Figure 2.2 Characteristics of EBUS images[14].	7
Figure 3.1 Samples of EBUS images: (a) and (b) are malignant, (c) and (d) are benign.	14
Figure 3.2 Flowchart of the proposed method.	15
Figure 3.3 Samples of the intersections between the ring area and the boundary of lesions are presented on the top row where the boundary of a lesion of each image is presented in red and the boundaries of the ring are presented in green. The ROIs are presented on the bottom row.	16
Figure 3.4 Histograms of EBUS images obtained from different gamma values.	17
Figure 3.5 Samples of WOIs in (a) malignant lesion and (b) benign lesion, where yellow, green, blue, and red squares represent W_{P5} , W_{P50} , W_{P95} , W_{100} , respectively.	18
Figure 3.6 An example of an 8-bit grayscale image with its GLCM.	20
Figure 3.7 The elements of the upper (red) and the lower (green) triangular GLCM when δ is set to 2.	21
Figure 3.8 (a) A sample of malignant lesion that was misclassified as benign. (b) A sample of benign lesion that was misclassified as malignant.	31
Figure 3.9 Samples of (a) benign lesion that looks similar to malignant lesion and (b) malignant lesion that looks similar to benign lesion.	31
Figure 4.1 Examples of different pulmonary lesion patterns in EBUS images: (a) benign lesion; (b) malignant lesion (benign and malignant lesions were confirmed after core needle biopsy).	44
Figure 4.2 The framework of the proposed pulmonary lesion classification system.	45
Figure 4.3 Data augmentation for malignant and benign images.	46
Figure 4.4 Results from the preprocessing step: (a) Original images; (b) mask images; (c) regions of interest; (d) WOIs in the intersection area of the region of interest and the ring.	48
Figure 4.5 Heat map of Pearson correlation coefficient matrix for all features.	49
Figure 4.6 Block diagram of the radiomics feature and patient data-based model.	50
Figure 4.7 The architecture of the fine-tuned DenseNet 169 for the single image-based model.	52

Figure 4.8 The architecture of the multi-patch-based model.....	53
Figure 4.9 The architecture of the proposed CNN in the multi-patch-based model.....	53
Figure 4.10 Weights learned by the first convolutional layer.....	55
Figure 4.11 (a) The original EBUS image; (b) the histogram of (a); (c) the enhanced EBUS image; (d) the histogram of (c).....	58
Figure 4.12 Feature selection of radiomics feature and patient data-based model.....	59
Figure 4.13 Confusion matrices:(a) the radiomics feature and patient data-based model; (b) the single image-based model; (c) the multi-patch-based model, and (d) the proposed framework.	61
Figure 4.14 Misclassification of the radiomics feature and patient data-based model: (a) malignant lesion was misclassified as benign; (b) benign lesion was misclassified as malignant.....	62
Figure 4.15 Misclassification of the single image-based model: (a) malignant lesion was misclassified as benign; (b) benign lesion was misclassified as malignant.....	63
Figure 4.16 Misclassification of the multi-patch-based model: (a) malignant lesion was misclassified as benign; (b) benign lesion was misclassified as malignant.....	64
Figure 4.17 Two out of three models misclassified a lesion, but the proposed framework can classify correctly. (a) benign lesion was misclassified as malignant in radiomics feature and patient data-based model and multi-patch-based model. (b) benign lesion was misclassified as malignant in single image-based model and multi-patch-based model.	65
Figure 4.18 ROC curves and AUC values of the classification models.....	66
Figure 5.1 Comparison graph of MI scores for the radiomics feature and patient data-based model.....	74
Figure 5.2 Examples of augmented test EBUS image data.....	75
Figure 5.3 The confusion matrices of the proposed framework with augmented test data:(a) the radiomics feature and patient data-based model; (b) the single image-based model; (c) the multi-patch-based model, and (d) the proposed framework.....	76

CHAPTER 1

INTRODUCTION

1.1 Statement of The Problem

Lung cancer is the second most common cancer in men according to the report of the global cancer statistics [1] while breast cancer is the most common cancer in women. Although lung cancer is the second most common cancer, it is the most common cause of cancer death [2]. Each year, lung cancer causes more deaths than colon and breast cancers combined. In Thailand, lung cancer is also the second most common cancer after liver cancer [3]. Lung cancer is the most common cause of cancer death because more than half of lung cancer patients die within a year of being diagnosed [4]. Lung cancer survival rates differ based on the stage of the disease at the time of diagnosis [5]. Lung cancer rarely causes symptoms in its early stages but there will be signs once the cancer has spread. There are many procedures for lung cancer screening [6-9], including X-rays, computed tomography (CT), bronchoscopy, pulmonary function studies (PFT), positron emission tomography (PET), low-dose computed tomography (LDCT), and other procedures. The diagnosis is confirmed by biopsy, which is usually performed by bronchoscopy or CT guidance [10].

A bronchoscopy [9] is a procedure in which a bronchoscope is inserted into the patient's nose or mouth by the doctor. The forceps take a sample of tissue from a lesion after the bronchoscope has reached the lesion. This is referred to as a biopsy. The tissue sample will be sent to a lab for testing to determine whether or not the cells are cancerous. CT and fluoroscopy are used to locate the lesion during surgery to locate it however, they are very harmful because the patients have to expose to radiation. In contrast, recent research discovered that bronchoscopy is guided by endobronchial ultrasonography [11] (EBUS) can help physicians diagnose the disease with a high percentage of accuracy, which is higher than conventional CT or fluoroscopy. The bronchoscope with EBUS can be used to visualize the internal surface

at a time by transmitting ultrasonic waves through the bronchioles and receiving their echoes by sending ultrasonic waves through the bronchioles to create a video of textures. EBUS is currently used for lung cancer diagnosis and staging, and it is considered a recommended standard in general practice [12] due to its high sensitivity and specificity [13]. The texture of a lesion is associated with pathology, in addition to the benefits of EBUS from visualizing the texture of a lesion. As a result, this knowledge can be applied to the development of a classification framework for diagnosing lesions. If the framework is accurate enough, it can reduce the need for biopsies, make the framework less reliant on humans, and shorten the time it takes to diagnose lung lesions.

Nowadays, pulmonary lesion classification is still an interesting research topic to be explored. The EBUS images have been used to classify pulmonary lesions and guide transbronchial needle aspiration. However, the final diagnostic decision depends on the pathological evidence. Although a lot of research has been conducted on the relationship between the characteristics of EBUS lesions and pathology, only a little research on the diagnostic tools for differentiating lesions has been conducted. As a result, the purpose of this research is to develop a pulmonary lesion classification framework for EBUS images.



1.2 Objectives

1. To derive new features from medical knowledge for lesion classification to improve the performance of classification.
2. To develop a pulmonary lesion classification framework for endobronchial ultrasonography images using machine learning

1.3 Scopes of Study

In this research, there are constraints as follows:

1. The input data consists of an EBUS video and patient data such as gender, age, smoking history, and lesion size.
2. It is assumed that when the bronchoscope reaches the lesion, the EBUS capture video begins to record.
3. The type of pulmonary lesion is divided into only two classes: benign and malignant.

1.4 Contributions

This research has two primary contributions. First, the new features called the adaptive weight sum of the lower and the upper GLCM features, which can be used to classify pulmonary lesions, are proposed. Second, the pulmonary lesion classification framework is proposed. The classification framework together with the proposed features for EBUS images can improve the accuracy and reduce time in preliminary diagnosis.

1.5 Organization of The Dissertation

The dissertation is structured as follows:

Chapter 1 explains briefly the statement of the problem, objectives, scope of study, and contributions.

Chapter 2 describes the related background knowledge and literature review.

Chapter 3 provides the details of Article 1: “Pulmonary Lesion Classification from Endobronchial Ultrasonography Images Using Adaptive Weighted-Sum of the Upper and Lower Triangular Gray-Level Co-Occurrence Matrix”.

Chapter 4 provides the details of Article 2: “Pulmonary Lesion Classification Framework using the Weighted Ensemble Classification with Random Forest and CNN Models”

Chapter 5 discusses and concludes the dissertation.

1.6 The Connection between Articles

The main objective of this dissertation is to determine from EBUS images whether pulmonary lesions are benign or malignant. The dissertation includes two previously published articles. All the articles are part of the graduation dissertation dissemination. Article 1 describes the proposed feature extraction for pulmonary lesion classification. The proposed features can be used to measure the heterogeneity of patterns of lesions in EBUS images, which is one of the most common characteristics of malignant. Article 2 describes the pulmonary lesion classification framework that uses the weighted ensemble classification to integrate three models and also the proposed features in article 1 to improve classification performance.

1.7 Expected Outcomes

1. The pulmonary lesion classification framework can be used to classify pulmonary lesions from EBUS images with an acceptable accuracy rate using an imbalanced and small dataset.
2. The pulmonary lesion classification framework is expected to assist radiologists in planning the preliminary treatment process.

CHAPTER 2

PULMONARY LESION CLASSIFICATION FRAMEWORK

This dissertation is divided into two parts. First, the new features for pulmonary lesion classification are proposed. Second, the pulmonary lesion classification framework that uses the proposed features in the first part together with other standard features is presented. Each part is described briefly below:

Article 1: Pulmonary Lesion Classification from Endobronchial Ultrasonography Images Using Adaptive Weighted-Sum of The Upper and Lower Triangular Gray-Level Co-Occurrence Matrix

Visual classification of pulmonary lesions from endobronchial ultrasonography (EBUS) images is performed by radiologists which may cause the results to be subjective. Therefore, two robust features, called the adaptive weighted-sum of the upper triangular gray-level co-occurrence matrix (AWSU) and the adaptive weighted-sum of the lower triangular gray-level co-occurrence matrix (AWSL), were proposed. These two features are combined with 22 other standard features and used as initial input data to the proposed classification method to assist the radiologists. The proposed method integrates the k^{th} percentile of the sum of intensities, genetic algorithm (GA), and support vector machine (SVM) to classify a lesion, and then applied the k^{th} percentile of the sum of intensities to select the optimal window of interest (WOI) where all the features are extracted. After feature extraction, GA is used to select only relevant features that are then forwarded to SVM to classify the lesion.

Efficiency of the proposed features and the proposed method was evaluated using a dataset of 89 EBUS images with 10-fold cross-validation. Optimal classification results were obtained using 16 selected features from the WOI at the 5th percentile with accuracy, sensitivity, specificity, and precision at 86.52%, 87.27%, 85.29%, and 90.57%, respectively. Among these 16 selected features, six of them were selected from the proposed features. The proposed method was compared with other existing methods and the results reveal that the proposed features together with the proposed

method can significantly improve the pulmonary lesion classification performance, especially for small datasets. Details of article 1 are described in Chapter 3.

Article 2: Pulmonary Lesion Classification Framework using the Weighted Ensemble Classification with Random Forest and CNN Models for EBUS Images

Lung cancer is a deadly disease with a high mortality rate. Endobronchial ultrasonography (EBUS) is one of the methods for detecting pulmonary lesions. Computer-aided diagnosis of pulmonary lesions from images can help radiologists to classify lesions; however, most of the existing methods need a large volume of data to give good results. Thus, this paper proposes a novel pulmonary lesion classification framework for EBUS images that works well with small datasets. The proposed framework integrates the statistical results from three classification models using the weighted ensemble classification. The three classification models include the radiomics feature and patient data-based model, the single-image-based model, and the multi-patch-based model. The radiomics features are combined with the patient data to be used as input data for the random forest, whereas the EBUS images are used as input data to the other two CNN models.

The performance of the proposed framework was evaluated on a set of 200 EBUS images consisting of 124 malignant lesions and 76 benign lesions. The experimental results show that the accuracy, sensitivity, specificity, positive predictive value, negative predictive value, and area under the curve are 95.00%, 100%, 86.67%, 92.59%, 100%, and 0.9333, respectively. This framework can significantly improve the pulmonary lesion classification. Details of article 2 are described in Chapter 4.

In general, EBUS images have details such as hospital number, name, age, gender, recorded time, position of lesion in lung, the range of frequency and the zooming distance as shown in Figure 2.1. The patient details were removed in the preprocessing step.

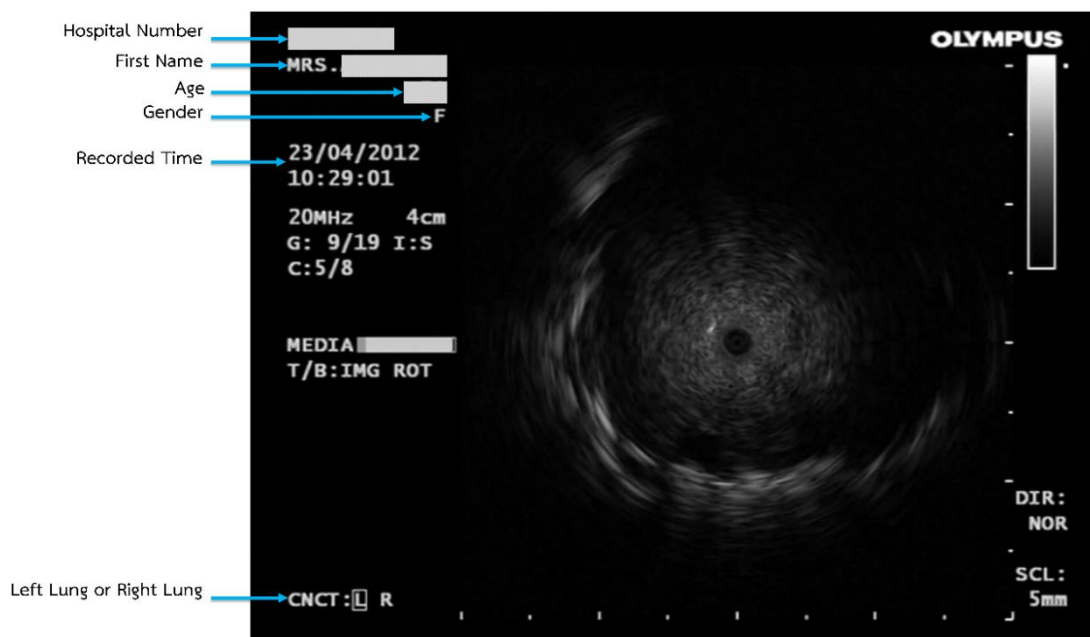


Figure 2.1 Sample of an EBUS image.

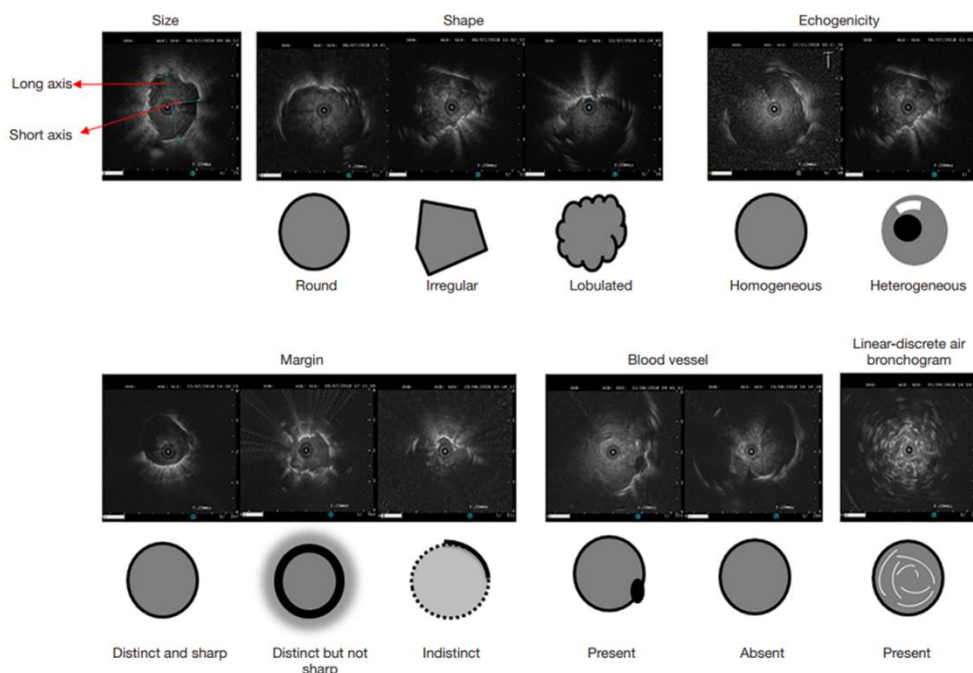


Figure 2.2 Characteristics of EBUS images[14].

Figure 2.2 depicts sample characteristics of EBUS images that are the most important features for classification. These characteristics are size, shape, echogenicity, margin, blood vessel, and linear-discrete air bronchogram. Long axis, lobulation,

distinct margin but not sharp margin, absence of blood vessel, and absence of linear-discrete air bronchogram were all found to be good predictors of malignant lesions in the study [14]. The echogenicity, size, and shape of EBUS images are also considered to be one of the factors that differentiates malignant from benign lesions in this dissertation.

Table 2.1 shows the difference between Articles 1 and 2. Article 1 input data consists solely of EBUS images, whereas Article 2 input data combines both EBUS images and patient data. In Article 1, there are 89 input data: 34 benign and 55 malignant. In Article 2, there are 200 input data: 76 benign and 124 malignant. Article 1 uses SVM classifiers, whereas Article 2 uses a weighted ensemble classification of three classifiers. Article 1's train-test scheme is 10-fold cross-validation. Article 2's train-test scheme is an 80/20 train-test split.

Table 2.1 The difference between Article 1 and Article 2.

	Article 1	Article 2
Input data	EBUS images	EBUS images and patient data
Number of input data	89 Benign: 34 Malignant: 55	200 Benign: 76 Malignant: 124
Recorded time	2015 to 2016	2011 to 2016
Classifiers	SVM	Combination of three classifiers 1. RF 2. Fine-tuned ResNet169 3. Proposed CNN
Train-test scheme	10-fold cross validation	80/20 train-test split

CHAPTER 3

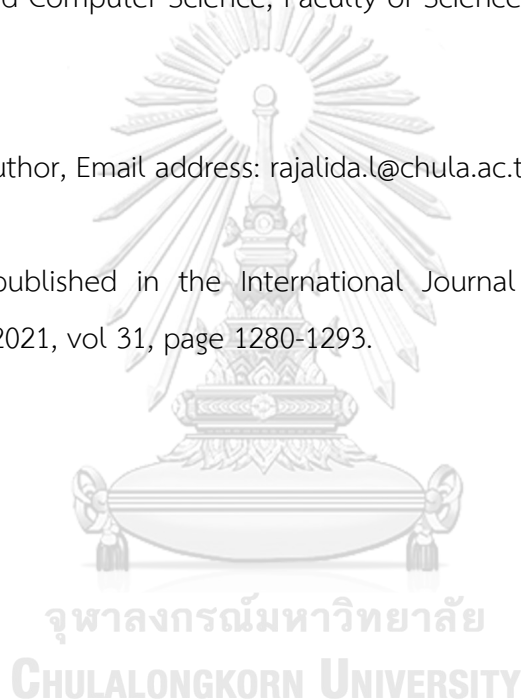
PULMONARY LESION CLASSIFICATION FROM ENDOBRONCHIAL
ULTRASONOGRAPHY IMAGES USING ADAPTIVE WEIGHTED-SUM OF THE
UPPER AND LOWER TRIANGULAR GRAY-LEVEL CO-OCCURRENCE MATRIX

Banphatree Khomkham and Rajalida Lipikorn*

Machine Intelligence and Multimedia Information Technology Laboratory, Department
of Mathematics and Computer Science, Faculty of Science, Chulalongkorn University,
Bangkok, Thailand

* Corresponding author, Email address: rajalida.l@chula.ac.th

This paper was published in the International Journal of Imaging Systems and
Technology, year 2021, vol 31, page 1280-1293.



Received: 22 January 2020

Revised: 12 October 2020

Accepted: 18 October 2020

Published: 1 November 2020

ABSTRACT

Visual classification of pulmonary lesions from endobronchial ultrasonography (EBUS) images is performed by radiologists; therefore, results can be subjective. Here, two robust features, called the adaptive weighted-sum of the upper triangular gray-level co-occurrence matrix (AWSU) and the adaptive weighted-sum of the lower triangular gray-level co-occurrence matrix (AWSL), were combined with 22 other standard features and used as initial input data to assist radiologists. The proposed method integrated the k th percentile of the sum of intensities, a genetic algorithm (GA), and support vector machine (SVM) to classify a lesion, and then applied the k th percentile of the sum of intensities to select the optimal window of interest (WOI) where all the features are extracted. After feature extraction, a GA was used to select only relevant features that were then forwarded to SVM to classify the lesion. Efficiency of the proposed features and the proposed method was evaluated using a dataset of 89 EBUS images with 10-fold cross-validation. Optimal classification results were obtained using 16 selected features from the WOI at the 5th percentile with accuracy, sensitivity, specificity, and precision at 86.52%, 87.27%, 85.29%, and 90.57%, respectively. Among the 16 selected features, six were from the proposed features. The proposed method was compared with other existing methods. Results revealed that the proposed features together with the proposed method significantly improved the classification performance of pulmonary lessons, especially for small datasets.

KEYWORDS: Gray-level co-occurrence matrix, genetic algorithms, support vector machine, adaptive weighted-sum of the upper triangular gray-level co-occurrence matrix, and adaptive weighted-sum of the lower triangular gray-level co-occurrence matrix.

3.1 Introduction

Lung cancer has the highest global mortality [1, 2], with five-year survival rates lower than many other leading cancer types [3]. Mortality rate can be reduced if lung

cancer is detected at an early stage. In 2012, Fontana et al. found that early detection of lung cancer and effective treatment can improve survival rate to at least 5 years [4].

Many different methods are available to diagnose lung cancer [5-7]. Among them, endobronchial ultrasonography is of benefit since the patient is not subjected to radiation and biopsy can be easily performed [8, 9]. There are many articles on the use of computer-aided diagnosis (CAD) for detecting cancer [10-15]; however, only a few are related to the EBUS technique. EBUS can play an important role in diagnosis when integrated with CAD to help a radiologist make the first decision faster and instigate timeous treatment and clinical practice.

Several articles [16-18] on peripheral pulmonary lesion classification reveal that one of the most prominent characteristics of EBUS that indicates malignancy is a heterogeneous pattern. This pattern can be determined using texture analysis on EBUS images. Texture analysis measures features that can be used to identify textural characteristics such as gray-level co-occurrence matrix, run-length matrix, and first-order descriptive features. Gray-level co-occurrence matrix (GLCM), first proposed by Haralick et al. [19] in 1973 is one of the most widely used methods for texture analysis in many fields including medicine [20-22], industry [23-25], and material [26-28].

Haralick et al. [19] proposed a set of 28 textural features that required uncomplicated computation based on GLCM, such as energy, homogeneity, contrast, correlation, inverse difference moment, sum average, and entropy. Each feature represented a unique characteristic, for example, contrast represented the difference in luminance and entropy represented intensity irregularity. Haralick's features have been widely exploited in radiomics studies [29] because radiomics data contain first-order features, second-order features, and higher-order features. The concept of radiomics involves extracting a large number of features from radiographic medical images using data-characterization algorithms. In 1980, Connors and Harlow [30] analyzed all 28 features proposed by Haralick and stated that only five were sufficient for classification. These five standard features of GLCM are now widely used in texture analysis as energy, entropy, contrast, homogeneity, and correlation. However, these standard features do not work for all types of images because each image is unique. The five features are suitable for general typical images but do not work in special

cases. Thus, identifying the characteristics and generating the associated features for special types of images are important for accurate image classification.

In 1992, Wu et al. [31] presented a classification of ultrasonic liver images using textural features such as spatial gray-level dependence matrices, the Fourier power spectrum, gray-level difference statistics, and Laws' texture energy. Their classification was evaluated on a set of 90 samples consisting of 30 samples of normal liver, 30 samples of hepatoma, and 30 samples of cirrhosis. The Bayes classifier and the Hotelling trace criterion were used to calculate the effect of features. Results revealed that accuracy was not high, with long time complexity. To resolve these problems, they presented the multiresolution fractal feature set as a robust solution to better classify ultrasonic liver images.

In 2002, Gomez et al. [32] presented an analysis of co-occurrence texture statistics as a function of gray-level quantization for classifying breast ultrasound. They considered 22 features from six different gray-scale quantization levels using the minimal-redundancy-maximal-relevance criterion to rank the dependency of the features. Their results showed that contrast and correlation features calculated from GLCM, with 90-degree orientation and distance of more than five pixels, could be used to significantly distinguish breast lesions.

In 2003, Lee et al. [33] proposed the feasibility of selecting a fractal feature vector based on M-band wavelet transform to classify ultrasonic liver images as normal, cirrhosis, or hepatoma. Their classification revealed that the fractal feature vector based on M-band wavelet transform was trustworthy. In 2013, Yang et al. [34] presented a robust texture analysis using multi-resolution gray-scale invariant features via ranklet transform for breast sonographic tumor diagnosis, while in 2016, Chong et al. [35] proposed the novel Robustness-Driven Feature Selection (RDFS) algorithm that preferentially selected features that were robust to variations in computed tomography (CT) technical factors. They evaluated RDFS as a CT classification of fibrotic interstitial lung disease using 3D textural features. In 2009, Drukker et al. [10] demonstrated the feasibility of a computerized auto-assessment method in which a computer-aided diagnosis system provided the level of confidence for its probability estimation of malignancy for each radiologist-identified lesion. In 2015, Zang et al.

presented image segmentation methods for 2D EBUS frames and 3D EBUS sequences by adapting the fast-marching level-set process, anisotropic diffusion, and region growing [36]. Ortiz et al. [37] used a genetic algorithm to select features of magnetic resonance (MR) brain images and applied self-organizing maps (SOM) to evaluate the fitness function in each iteration of the GA to minimize the quantization and topological errors. Militello et al. [38] proposed a segmentation method based on an Unsupervised Possibilistic Fuzzy C-means clustering algorithm to segment tumors and calculate lesion volume to improve the performance of brain tumor diagnosis. In our previous work, we proposed two features for pulmonary lesion classification called the weighted-sum of lower and upper GLCM [39]. These two features were combined with 22 standard features, and a GA was used to select only the relevant features. Results revealed that a combination of the proposed and standard features improved the accuracy. Rundo et al. [40] proposed a framework for MR image segmentation by enhancing an image using MedGA to improve the threshold selection between the underlying subdistributions based on a GA. The MedGA outperformed other state-of-the-art methods in terms of signal and perceived image quality while preserving input mean brightness.

Recently, deep learning (DL) has become the foundation of medical imaging to assist radiologists in clinical diagnosis and support their clinical decisions. For example, convolutional neural networks (CNN) were used to detect lung nodules in CT images [41, 42], and the dense convolutional binary-tree network for lung nodule classification from CT images was proposed by Liu et al. [43]. However, DL is suitable for a large volume of data, while its performance declines if the dataset is too small. According to the review of Alom et al. [44], traditional machine learning has better performance for small volume of data but the performance of DL turns to be better than the performance of traditional machine learning when the volume of data increases to some certain size.

Thus, here, we propose a new method with new features that can effectively and efficiently classify lesions regardless of the volume of data. Two new features are proposed called the adaptive weighted-sum of the upper triangular gray-level co-occurrence matrix and the adaptive weighted-sum of the lower triangular gray-level

co-occurrence matrix to determine heterogeneity, which is one of the most important characteristics of malignancy [16, 18, 39]. The proposed method integrates window of interest selection, a genetic algorithm and support vector machine to classify a lesion using the proposed features with 22 other standard features as input data.

This paper is organized as follows. Section 2 describes the materials and section 3 introduces the proposed features and the proposed method. Section 4 presents the classification results, while section 5 outlines the conclusions.

3.2 Materials

EBUS image data were collected from 2015 to 2016 at Phramongkutklo Hospital, Bangkok, Thailand. Endobronchial ultrasonography was performed by expert radiologists. An endoscopic ultrasound system (EU-ME1; Olympus) and a 20 MHz miniature radial probe (UM-S20-17S; Olympus) were used to obtain the EBUS images. The probe provided a panoramic ultrasonic view (360 °) of a lesion. EBUS videos were recorded and saved in the form of video files (.mod). These were transformed to .mp4 files at the rate of 30 frames/second. Then, high quality frames that contained lesions with diameter 3-12 mm were extracted from each video file and saved as an 8-bit grayscale image in .jpg file format with size 776×776 pixels and no metadata (name, hospital number, age, gender, etc.) as shown in Figure 3.1 The EBUS image dataset contained 89 images of pulmonary lesions; 55 were malignant and 34 were benign.

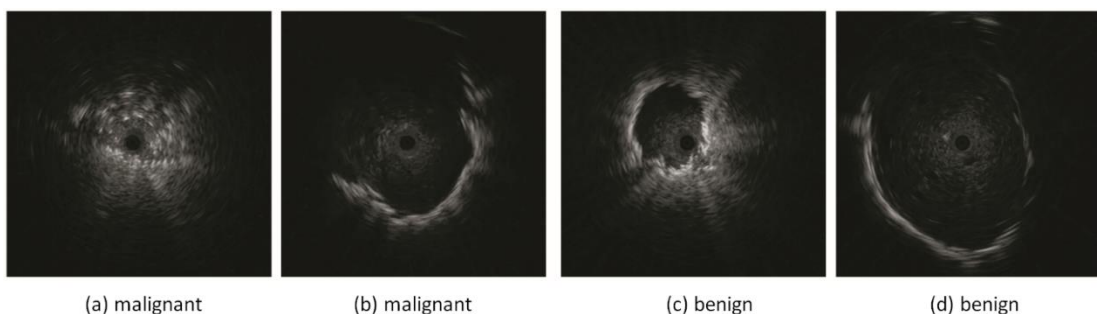


Figure 3.1 Samples of EBUS images: (a) and (b) are malignant, (c) and (d) are benign.

3.3 Methods

The proposed method consisted of five steps as preprocessing, window of interest selection, feature extraction, feature selection, and lesion classification. A flowchart of the proposed method is shown in Figure 3.2 Each step is explained below, followed by a performance evaluation.

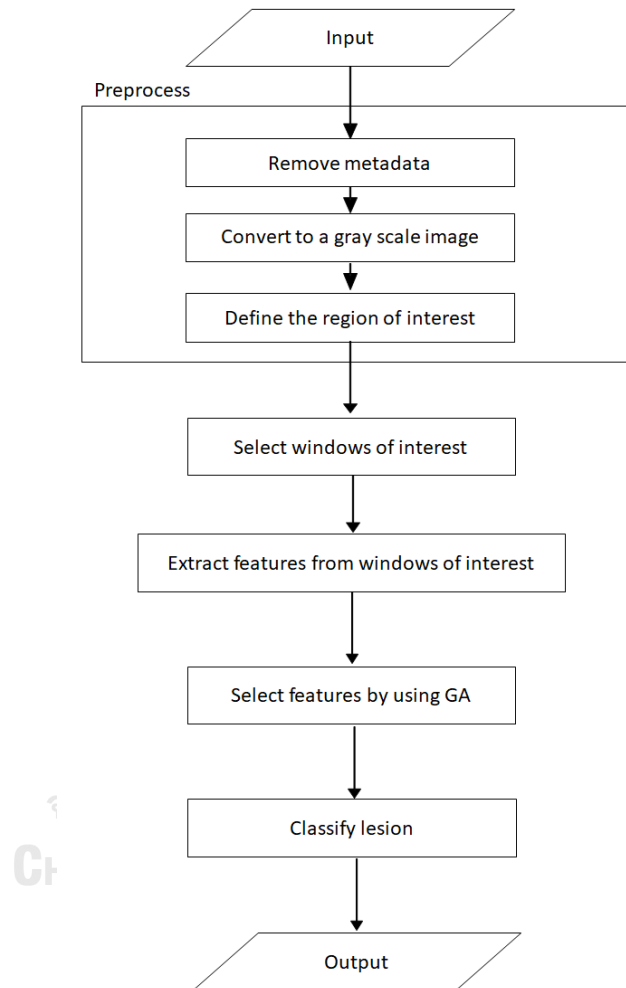


Figure 3.2 Flowchart of the proposed method.

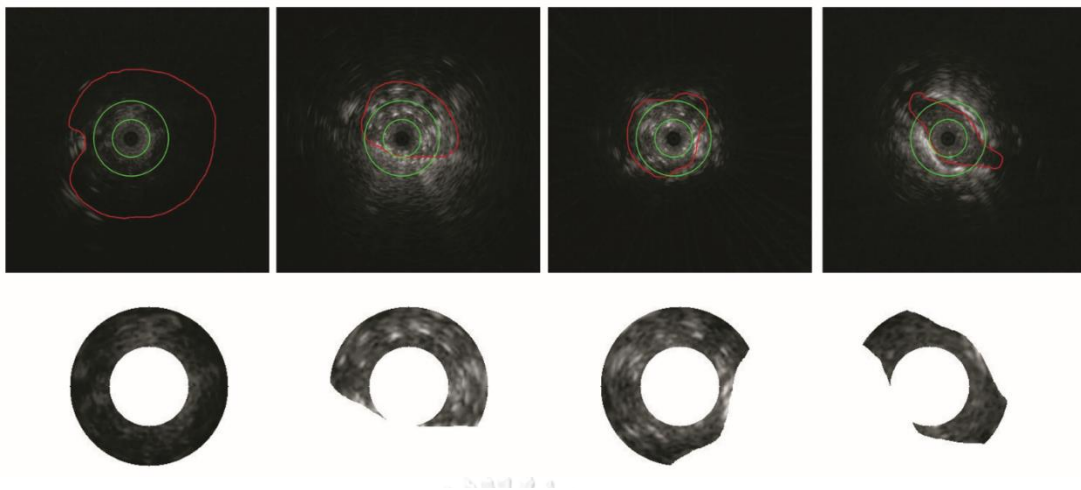


Figure 3.3 Samples of the intersections between the ring area and the boundary of lesions are presented on the top row where the boundary of a lesion of each image is presented in red and the boundaries of the ring are presented in green. The ROIs are presented on the bottom row.

3.3.1 Preprocessing

The original images obtained from the video contained regions that were not relevant to lesion classification such as metadata, background, air, noise, and the probe. These regions were not included in the classification process because they can decrease performance. According to Kurimoto et al. [18], the most suitable region for lesion diagnosis is the area inside a ring with distance between 3 mm and 5 mm from the probe. Thus, the first preprocessing step was to automatically identify this ring according to Kurimoto's definition after each EBUS image was converted from RGB to grayscale. However, the shape of a lesion was usually irregular and, therefore, the ring might cover regions outside the lesion. Therefore, the lesion boundary was either manually defined by a radiologist or automatically defined by the polar sector maximum intensity method [45]. After the ring and lesion boundary were defined, the region of interest (ROI) containing classification features was defined as the intersection between the area inside the boundary of the lesion and the area of the ring, as shown in Figure 3.3 The boundary of the lesion is shown in red, whereas the boundary of the ring is presented in green. The ROI of each image is located on the bottom row. The

next task involved gamma correction to adjust the image contrast because most of the original EBUS images were too dark. The gamma was set to 0.5 ($\gamma=0.5$) because the air inside a lesion is represented as a dark region with very low intensity. These regions should be kept dark, while other components should be enhanced brighter to visualize the lesion texture. The histograms in Figure 3.4 show $\gamma=0.5$ as the optimal setting because the dark regions remained dark, while the other regions became brighter but not too bright.

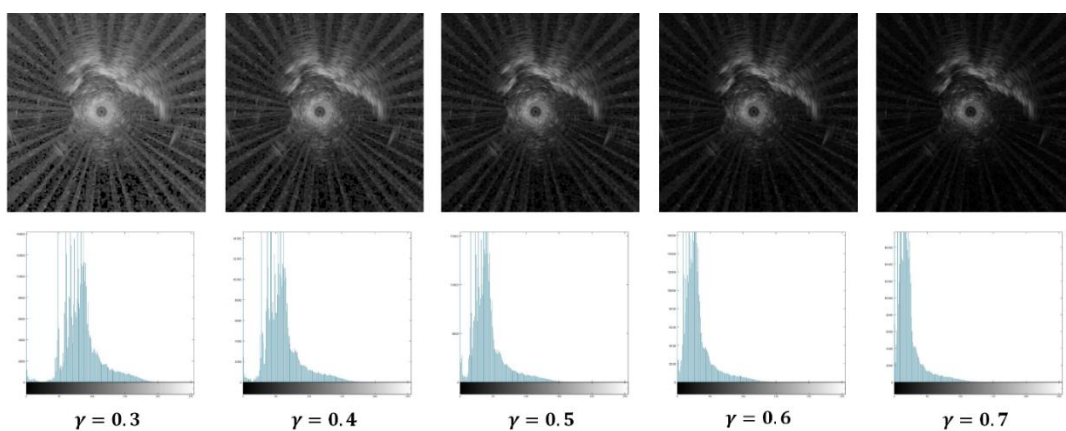


Figure 3.4 Histograms of EBUS images obtained from different gamma values.

3.3.2 Window of Interest Selection

After the ROI was obtained, the next step was to determine the WOI as the largest square that could fit within the ROI containing the area for lesion diagnosis. The area inside the ROI may contain other components, such as fluid and air that can cause an inaccurate diagnosis. Thus, an effective method was proposed to select the WOI as follows:

1. Define a window of size $n_w \times n_w$ to be the largest window that can fit within the ROI
2. Place the window at the upper-left position of the ROI, where the entire window is inside the ROI
3. Compute the sum of intensities of the region inside the window
4. Shift the window m pixels to the right where m can be any constant value, and repeat step 3 - step 4 until reaching the boundary of the ROI

5. Shift the window down m pixels and move it to the left of the ROI, then repeat step 3 - step 5 until covering the entire ROI

The WOIs of each image are selected from the windows whose sum of intensities are 5, 50, 95, and 100 percentiles.

$$WOI_{img} = \{W_{P5}, W_{P50}, W_{P95}, W_{P100}\} \quad (1)$$

where WOI_{img} represents a set of WOIs of each image, W_{Pk} represents a window at percentile k , and $k = \{5, 50, 95, 100\}$. Examples of WOIs selected from benign and malignant lesions are shown in Figure 3.5.

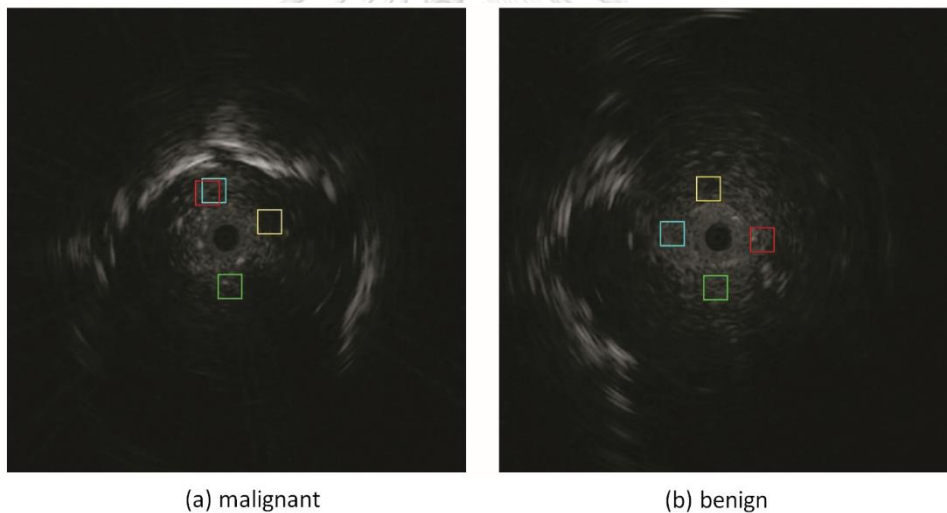


Figure 3.5 Samples of WOIs in (a) malignant lesion and (b) benign lesion, where yellow, green, blue, and red squares represent $W_{P5}, W_{P50}, W_{P95}, W_{P100}$, respectively.

3.3.3 Feature Extraction

Features are very useful in pattern recognition since they contain a lot of information that is hidden in an image. Features can also be used to represent characteristics of an image and they can be extracted from an image in many different ways. GLCM is a statistical method that determines the spatial relationship of pixels by

counting the occurrences of pairs of pixels with specific intensities in a specified orientation. The elements along the diagonal line of GLCM represent pairs of pixels with similar intensities that exemplify homogeneity characteristics. On the other hand, the elements that are further away from the diagonal line represent pairs of pixels with different intensities. The elements further away from the diagonal line have increasingly different intensities. Thus, if the elements close to the diagonal line have higher values than those further away, this can be interpreted as having a high chance of being homogeneous as one of the standard features of GLCM.

This paper proposes two new robust features that can be used to determine the heterogeneity of a lesion called the adaptive weighted-sum of the lower triangular GLCM and the adaptive weighted-sum of the upper triangular GLCM. The AWSL and AWSU focus on the elements in the lower and upper triangular GLCM because these elements contain heterogeneity characteristics. To accentuate the heterogeneity characteristics, the elements along the diagonal line with the specified cutoff value are not included in the proposed features, while the elements of GLCM are weighted by the difference between intensities of two pixels. Moreover, these two features use the characteristics of GLCM to help distinguish homogeneity characteristics from heterogeneity characteristics in the weight setting. The AWSL and AWSU are defined in equations (2)-(4).

$$AWSL(d, \theta) = \sum_{i=\delta}^{n-1} \sum_{j=0}^{i-\delta-1} W_{ij} P(i, j, d, \theta) \quad (2)$$

$$AWSU(d, \theta) = \sum_{i=0}^{n-1} \sum_{j=i+\delta-1}^{n-1} W_{ij} P(i, j, d, \theta) \quad (3)$$

where n is the number of gray-levels, δ is the cutoff value which defines the width of the diagonal line where the elements of GLCM are not taken into consideration, $P(i, j, d, \theta)$ is the element of GLCM, d is the shifting distance to the adjacent pixel, θ is the orientation, and W_{ij} is the adaptive weight function at row i and column j that is defined as:

elements that are further away from the diagonal line usually have a value equal to 0. If the cutoff value is too large, a significant amount of the image information may be lost [46].

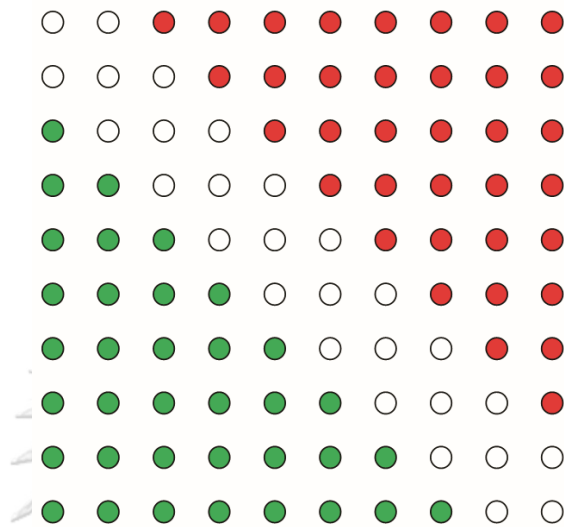


Figure 3.7 The elements of the upper (red) and the lower (green) triangular GLCM when δ is set to 2.

All preprocessing step and feature extraction operations were implemented using MATLAB 2018b. The extracted features were used for feature selection, while classification was implemented using Rapid Miner Studio 9.3.001 (Educational edition). All experiments were performed on a computer with Intel(R) CPU Core(TM) i7-3770K @3.50GHz, GPU NVIDIA GeForce GT630, and 8.00 GB of RAM.

3.3.4 Feature Selection

Thirteen standard features as standard deviation, skewness, kurtosis, variance, entropy, contrast, correlation, energy, homogeneity, mean, AWSL, AWSU, and AWS extracted from an image were forwarded to the next step for feature selection. The first three were the standard features used by Morikawa et al. [17], the next six were the standard features used by Haralick et al. [19], and the last three were the proposed features. The first five features including the mean were first-order features, while the

rest were second-order features. Among these, the second-order features were calculated from the GLCM that contained the distribution of co-occurring gray-level values in a specified orientation within a window. In this paper, four orientations were used to generate GLCMs for the second-order features at 0-degrees, 45-degrees, 90-degrees, and 135-degrees to obtain 28 features. These 28 features were combined with the first-order features to generate a feature vector of 34 features for each window, as shown in Table 3.1. Since the values of these features were in different ranges, all features were normalized to be between 0 and 1 before performing the classification. However, some of the features had less impact on lesion classification; thus, a genetic algorithm [47] was used for feature selection to select only relevant features and improve classification accuracy.

Table 3.1 Features that are used for lesion classification.

No	Feature
1	Mean
2	Variance
3	Standard deviation
4	Skewness
5	Kurtosis
6	Entropy
7	Contrast 0-degree
8	Contrast 45-degree
9	Contrast 90-degree
10	Contrast 135-degree
11	Correlation 0-degree
12	Correlation 45-degree
13	Correlation 90-degree
14	Correlation 135-degree
15	Energy 0-degree
16	Energy 45-degree
17	Energy 90-degree
18	Energy 135-degree
19	Homogeneity 0-degree

20	Homogeneity 45-degree
21	Homogeneity 90-degree
22	Homogeneity 135-degree
23	Adaptive weighted-sum of lower GLCM 0-degree
24	Adaptive weighted-sum of lower GLCM 45-degree
25	Adaptive weighted-sum of lower GLCM 90-degree
26	Adaptive weighted-sum of lower GLCM 135-degree
27	Adaptive weighted-sum of upper GLCM 0-degree
28	Adaptive weighted-sum of upper GLCM 45-degree
29	Adaptive weighted-sum of upper GLCM 90-degree
30	Adaptive weighted-sum of upper GLCM 135-degree
31	Adaptive weighted-sum of lower and upper GLCM 0-degree
32	Adaptive weighted-sum of lower and upper GLCM 45-degree
33	Adaptive weighted-sum of lower and upper GLCM 90-degree
34	Adaptive weighted-sum of lower and upper GLCM 135-degree

Genetic algorithms are used in artificial intelligence to search for optimized solutions by imitating the theory of natural selection and evolution [48]. GAs have the advantage of tolerating errors in finding solutions from complex and difficult data using mathematical equations.

The main components of a GA are chromosome encoding, population initialization, fitness function, selection, crossover, mutation, and replacement. Binary coding was used in the chromosome encoding step to represent the features of an EBUS image. Each chromosome was a string containing 34 bits of 0s or 1s and each bit or gene represented one of the 34 features. In the next step, the initial population consisting of chromosomes was selected by random initialization, with population size greater than or equal to the number of genes [49]. In this paper, population size was set to 34, following [49] which indicated that a GA should perform better with less time complexity for moderate population size. The fitness function was used to select a pair of chromosomes for reproduction based on accuracy maximization. A trained classifier was used as a fitness function. The GA iteration stopped when the fitness function no longer improved or when the maximum number of generations was

reached. The maximum number of generations was set to 500 because from trial and error no significant improvement occurred beyond this number. A tournament selection scheme was used to select the parents with tournament size equal to 0.25. The crossover was implemented through a uniform distribution with probability of 0.5 and the mutation operator also used uniform distribution with probability of $1/\text{number of features}$ [50]. Table 3.2 shows the details of parameter settings for the GA used in this paper.

Table 3.2 Genetic algorithm parameters.

GA parameter	Value
Encoding type	Binary vector
Population size	34
Crossover probability	0.5
Mutation probability	$1 / \text{number of features}$
Selection scheme	Tournament (tournament size = 0.25)
Crossover type	Uniform distribution
Mutation type	Uniform distribution

3.3.5 Lesion Classification

Next, the selected features were entered into four classifiers as k-nearest neighbors (KNN) [51], linear discriminant analysis (LDA) [52], SVM [53], and DL [54]. These four classifiers are widely used in medical image classification. For the KNN classifier, k was set equal to 2 using Euclidean distance to measure the similarity. For the SVM classifier, choosing an appropriate kernel function is important to obtain the optimal solution. The sigmoid kernel function is commonly used in support vector machines and proved to be an effective choice for comparing the performance with other kernel functions. Hence, we used the sigmoid function as a kernel function in SVM to find the optimal solution.

The robustness of the proposed features and the proposed method was demonstrated by comparing the classification results with those obtained from using DL for two sets of features. The architecture of the fine-tuned DL model for the

experiments consisted of two hidden layers with hyperbolic tangent function. The number of neurons in each hidden layer was set to $\frac{\text{number of features} + \text{number of classes}}{2} + 1$ [50].

3.3.6 Performance Evaluation

To compare the results with those obtained from existing methods in the medical field, sensitivity (Sen) and specificity (Spec), together with accuracy (Acc) and precision (Prec) were used to evaluate performance [55, 56]. Sensitivity was used to measure the ability of the proposed method to correctly identify the lesion as malignant and was calculated by

$$\text{Sen} = \frac{\text{TP}}{\text{TP} + \text{FN}} \quad (6)$$

where TP and FN represent the number of true positive and false negative values. Specificity was used to measure the ability of the proposed method to correctly identify a lesion as benign and was calculated by

$$\text{Spec} = \frac{\text{TN}}{\text{TN} + \text{FP}} \quad (7)$$

where TN and FP represent the number of true negative and false positive values. Accuracy was used to measure the true number of classifications and was calculated by

$$\text{Acc} = \frac{\text{TP} + \text{TN}}{\text{TP} + \text{TN} + \text{FN} + \text{FP}} \quad (8)$$

Precision was used to determine how precisely the proposed method could classify malignancy and was calculated by

$$\text{Prec} = \frac{\text{TP}}{\text{TP} + \text{FP}} \quad (9)$$

3.4 Experimental Results

The experiments were performed on a dataset of 89 images. Four different WOIs as P5, P50, P95, and P100, were selected from each image for feature extraction. The experiments were divided into three phases using four classifiers: KNN, LDA, SVM, and DL with 10-fold cross-validation and stratified sampling was used as the sampling method. The classification performance was measured by comparing the results obtained from the proposed method with those obtained from other methods. The first phase verified whether the proposed features were better than the features extracted from symmetric GLCM. The classification results using standard features, and proposed features were compared to those using only standard features, and results from using standard features and AWS that represented features from symmetric GLCM. In the first phase, the classifications were performed on three different sets of features using four classifiers with the GA. Table 3.3 shows the classification results using only 22 standard features, while Table 3.4 shows the classification results using 22 features with AWS and classification results using 22 features with AWSU and AWSL. The accuracy rate using the proposed method with 22 features, AWSU, and AWSL was 83.15% and better than the other methods.

The second and third phases compared the performance of the proposed method with other methods using all 34 features from four WOIs. To show that the GA improved the classification performance, experiments in the second phase were performed using the four classifiers without the GA, and experiments in the third phase were performed using the four classifiers with the GA. Results in Table 3.5 show that most of the methods recorded accuracy rates lower than 60% when the GA was not applied to select the features. However, after applying the GA for feature selection,

accuracy rates significantly improved, and results obtained from the proposed method using WOI at the 5th percentile outperformed the other methods. The accuracy rate obtained from the proposed method together with the proposed features was high at 86.52%. Table 3.6 shows the 16 features selected by the GA, including six of the proposed features, indicating that they were relevant to the characteristics of cancer.

Table 3.7 shows the classification results from a dataset of 89 EBUS images. Seven out of 55 malignant lesions were misclassified as benign, whereas only five out of 34 benign lesions were misclassified as malignant using the proposed features with the proposed method. Results in Table 3.7 yielded classification with 87.27% sensitivity, 85.29% specificity, and 90.57% precision. Moreover, accuracy rates in Table 3.8 verified that 0.5 was the optimal value for gamma. Figure 3.8(a) shows a malignant lesion that was misclassified as benign, while Figure 3.8(b) shows a benign lesion that was misclassified as malignant. Figure 3.9(a) shows a benign lesion that looked similar to a malignant lesion because it contained hyperechoic dots and linear arcs but it was correctly classified as benign. Figure 3.9(b) shows a malignant lesion that looked similar to a benign lesion because it had a homogeneous pattern, but it was correctly classified as malignant by the proposed method. On the other hand, the lesions in Figure 3.9 were misclassified when the GA was not used to select only the relevant features before performing the classification.

Table 3.3 Classification results obtained from four classifiers with GA using 22 features.

	Standard features			
	KNN	LDA	SVM	DL
P5	76.40%	70.79%	80.90%	71.91%
P50	68.54%	69.66%	73.03%	58.43%
P95	70.79%	69.66%	75.28%	65.17%
P100	71.91%	70.79%	79.78%	68.54%

Table 3.4 Classification results obtained from four classifiers with GA using standard features + AWS and standard features + AWSU+AWSL.

	Standard features + AWS				Standard features + AWSU+AWSL			
	KNN	LDA	SVM	DL	KNN	LDA	SVM	DL
P5	77.53%	74.16%	77.53%	68.54%	75.28%	75.28%	83.15%	70.79%
P50	73.03%	69.66%	79.78%	61.80%	71.91%	66.29%	78.65%	65.17%
P95	70.79%	73.03%	77.53%	59.55%	73.03%	67.42%	79.78%	64.04%
P100	76.40%	69.66%	79.78%	64.04%	76.40%	73.03%	79.78%	65.17%

Table 3.5 Classification results obtained from four classifiers with GA using 34 features.

	Without GA				With GA			
	KNN	LDA	SVM	DL	KNN	LDA	SVM	DL
P5	53.93%	49.44%	50.56%	61.80%	77.53%	75.28%	86.52%	70.79%
P50	56.18%	51.69%	42.70%	57.30%	73.03%	66.29%	78.65%	71.91%
P95	56.18%	47.19%	51.69%	55.06%	74.16%	69.66%	78.65%	59.55%
P100	61.80%	53.93%	43.82%	58.43%	78.65%	71.91%	76.40%	65.17%

Table 3.6 The selected features from P5 for SVM classifier.

The selected features for SVM with P5
Mean
Variance
Skewness
Contrast 0-degree
Contrast 45-degree
Correlation 45-degree
Energy 0-degree
Energy 135-degree
Homogeneity 0-degree
Homogeneity 90-degree
Adaptive Weighted-sum of lower GLCM 0-degree

Adaptive Weighted-sum of upper GLCM 0-degree
Adaptive Weighted-sum of lower and upper GLCM 0-degree
Adaptive Weighted-sum of lower GLCM 45-degree
Adaptive Weighted-sum of upper GLCM 45-degree
Adaptive Weighted-sum of upper GLCM 135-degree

Table 3.7 Confusion matrix of using GA and SVM with features from P5.

GA + SVM		
Classified as:	True:	
	Malignant	Benign
Malignant	48	5
Benign	7	29

Table 3.8 Comparison of accuracy obtained from different gamma values.

Gamma	Acc
0.1	79.78%
0.2	77.53%
0.3	82.02%
0.4	82.02%
0.5	86.52%
0.6	80.90%
0.7	79.78%
0.8	75.28%
0.9	83.15%
1.0	78.65%

3.5 Conclusions

This paper proposes two new features called AWSL and AWSU, together with a method for pulmonary lesion classification using a GA with SVM. From our previous work [39], WOI selection was improved by considering windows whose sum of intensities were at different percentiles. Two new features called the adaptive

weighted-sum of the lower triangular GLCM and the adaptive weighted-sum of the upper triangular GLCM were proposed. The first phase of the experiments showed that the proposed features were suitable for representing heterogeneity characteristics because they determined the differences between intensities by discarding the similarities of the elements along the diagonal line of GLCM. Combining the proposed features with standard features improved the performance of all classifiers. Furthermore, the second and the third phases of the experiments revealed that the performance of the classifiers could be improved further by applying the GA to select only features relevant to pulmonary lesion classification. Classification results showed that using more features did not guarantee better performance, while it was important to use only the right features. Results in Table 3.3 to Table 3.5 showed that the highest accuracy rate was obtained by using the proposed method to classify pulmonary lesions from a combination of standard features and proposed features. Moreover, the proposed method outperformed DL when the dataset was small. As a consequence, the proposed method was robust for pulmonary lesion classification, especially for small datasets.

Figure 3.8(a) shows a malignant lesion that was misclassified because its texture was homogeneous and the edges were very clear, very similar to the characteristics of a benign lesion. On the other hand, the benign lesion in Figure 3.8(b) was misclassified because its texture was not homogeneous. Even trained radiologists cannot be certain of their diagnoses for the images in Figures 3.8(a) and (b). They need to confirm their diagnoses by performing histopathology. Thus, pulmonary lesion classification can be significantly improved using the proposed features with the GA and SVM, giving an accuracy rate as high as 86.52%. Moreover, in terms of a quantitative comparison with our previous work, the accuracy rate of this proposed method improved from 84.27% to 86.52% and sensitivity improved from 82.53% to 87.27%. For future research, we aim to further improve the accuracy rate of the classification by developing new features and modifying the architecture of DL to make it more suitable for EBUS images. Moreover, segmentation of pulmonary lesions might be addressed by unsupervised approaches due to the small sample size of the analyzed dataset.

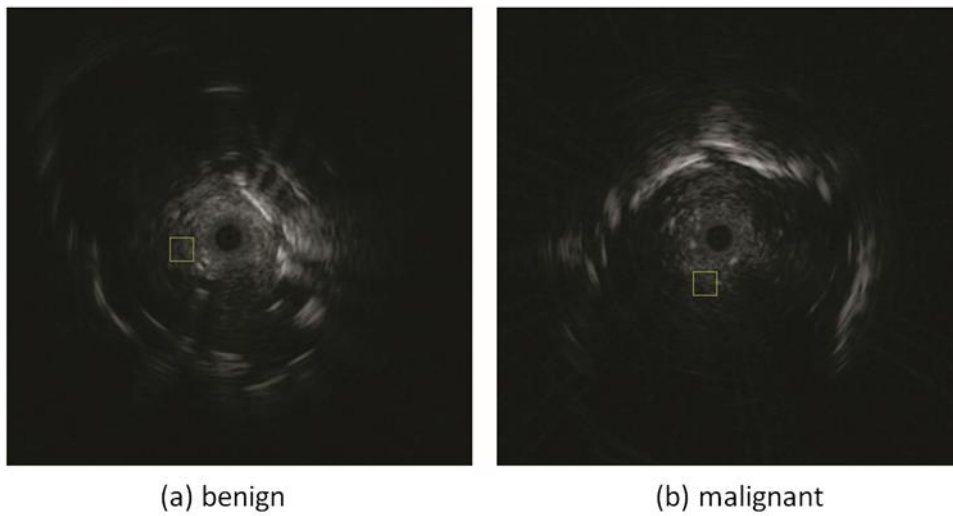


Figure 3.8 (a) A sample of malignant lesion that was misclassified as benign. (b) A sample of benign lesion that was misclassified as malignant.

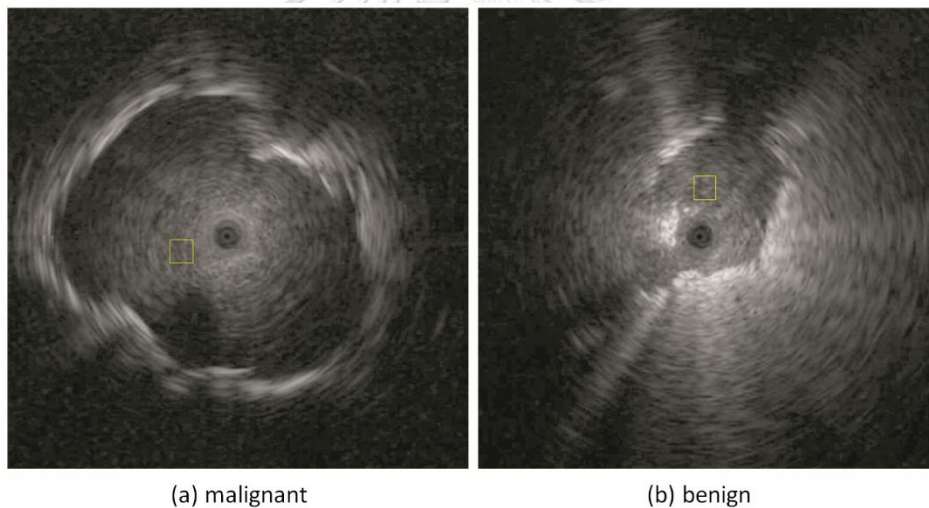


Figure 3.9 Samples of (a) benign lesion that looks similar to malignant lesion and (b) malignant lesion that looks similar to benign lesion.

Acknowledgment

The authors would like to thank Phramongkutklo Hospital, Bangkok, Thailand for providing EBUS data. Data availability is on request due to ethical restrictions. In particular, the authors would like to thank Maj.Gen. Dr. Anan Wattanathum, M.D. and

Dr. Jutamas Dechsanga, M.D. for verifying the results of best frame selection and boundary detection, and for providing the knowledge about lung cancer. This research has been supported by the Development and Promotion of Science and Technology Talent Project (DPST), under the administration of the Institute for the Promotion of Teaching Science and Technology (IPST), Thailand.

References

- [1] H. Rafiemanesh *et al.*, "Epidemiology, incidence and mortality of lung cancer and their relationship with the development index in the world," *Journal of Thoracic Disease*, vol. 8, no. 6, pp. 1094-1102, 2016, doi: 10.21037/jtd.2016.03.91.
- [2] R. L. Siegel, K. D. Miller, and A. Jemal, "Cancer statistics, 2016," *CA: a cancer journal for clinicians*, vol. 66, no. 1, pp. 7-30, 2016.
- [3] P. M. de Groot, C. C. Wu, B. W. Carter, and R. F. Munden, "The epidemiology of lung cancer," *Translational lung cancer research*, vol. 7, no. 3, pp. 220-233, 2018, doi: 10.21037/tlcr.2018.05.06.
- [4] R. S. Fontana *et al.*, "Early lung cancer detection: results of the initial (prevalence) radiologic and cytologic screening in the Mayo Clinic study," *American Review of Respiratory Disease*, vol. 130, no. 4, pp. 561-565, 1984.
- [5] M. Kaneko *et al.*, "Peripheral lung cancer: screening and detection with low-dose spiral CT versus radiography," *Radiology*, vol. 201, no. 3, pp. 798-802, Dec. 1996, doi: 10.1148/radiology.201.3.8939234.
- [6] D. R. Aberle *et al.*, "Reduced lung-cancer mortality with low-dose computed tomographic screening," *New England Journal of Medicine*, vol. 365, no. 5, pp. 395-409, 2011.
- [7] G. Sutedja, "New techniques for early detection of lung cancer," *The European respiratory journal Supplement*, vol. 39, pp. 57-66, Jan 2003, doi: 10.1183/09031936.03.00405303.
- [8] B. T and J. H. F, "Endobronchial ultrasound: a new innovation in bronchoscopy," *Lung India*, vol. 26, no. 1, pp. 17-21, Jan 2009, doi: 10.4103/0970-2113.45199.
- [9] K. Yasufuku, T. Nakajima, M. Chiyo, Y. Sekine, K. Shibuya, and T. Fujisawa, "Endobronchial ultrasonography: current status and future directions," *Journal of Thoracic Oncology*, vol. 2, no. 10, pp. 970-979, Oct 2007, doi: 10.1097/JTO.0b013e318153fd8d.
- [10] K. Drukker, C. A. Sennett, and M. L. Giger, "Automated method for improving system performance of computer-aided diagnosis in breast ultrasound," *IEEE Trans Med Imaging*, vol. 28, no. 1, pp. 122-128, Jan 2009, doi: 10.1109/TMI.2008.928178.

- [11] G. Han *et al.*, "The LISS--a public database of common imaging signs of lung diseases for computer-aided detection and diagnosis research and medical education," *IEEE Trans Biomed Eng*, vol. 62, no. 2, pp. 648-656, Feb 2015, doi: 10.1109/TBME.2014.2363131.
- [12] A. Meyer-Baese, O. Lange, T. Schlossbauer, and A. Wismuller, "Computer-aided diagnosis and visualization based on clustering and independent component analysis for breast MRI," in *Proc Int Conf Image Proc*, Oct 12, 2008. [Online]. Available: <https://www.ncbi.nlm.nih.gov/pubmed/19915691>.
- [13] H. R. Roth *et al.*, "Improving computer-aided detection using convolutional neural networks and random view aggregation," *IEEE Trans Med Imaging*, vol. 35, no. 5, pp. 1170-1181, May 2016, doi: 10.1109/TMI.2015.2482920.
- [14] H. C. Shin *et al.*, "Deep convolutional neural networks for computer-aided detection: CNN architectures, dataset characteristics and transfer learning," *IEEE Trans Med Imaging*, vol. 35, no. 5, pp. 1285-1298, May 2016, doi: 10.1109/TMI.2016.2528162.
- [15] T. Tan, B. Platel, R. Mus, L. Tabar, R. M. Mann, and N. Karssemeijer, "Computer-aided detection of cancer in automated 3-D breast ultrasound," *IEEE Trans Med Imaging*, vol. 32, no. 9, pp. 1698-1706, Sep 2013, doi: 10.1109/TMI.2013.2263389.
- [16] N. Kurimoto, M. Murayama, S. Yoshioka, and T. Nishisaka, "Analysis of the internal structure of peripheral pulmonary lesions using endobronchial ultrasonography," *Chest*, vol. 122, no. 6, pp. 1887-1894, Dec 2002, doi: 10.1378/chest.122.6.1887.
- [17] K. Morikawa, N. Kurimoto, T. Inoue, M. Mineshita, and T. Miyazawa, "Histogram-based quantitative evaluation of endobronchial ultrasonography images of peripheral pulmonary lesion," *Respiration*, vol. 89, no. 2, pp. 148-154, 2015, doi: 10.1159/000368839.
- [18] C. H. Kuo, S. M. Lin, H. C. Chen, C. L. Chou, C. T. Yu, and H. P. Kuo, "Diagnosis of peripheral lung cancer with three echoic features via endobronchial ultrasound," *Chest*, vol. 132, no. 3, pp. 922-929, Sep 2007, doi: 10.1378/chest.06-3106.
- [19] R. M. Haralick and K. Shanmugam, "Textural features for image classification," *IEEE Transactions on systems, man, and cybernetics*, no. 6, pp. 610-621, 1973.
- [20] M. B. Nagarajan, P. Coan, M. B. Huber, P. C. Diemoz, C. Glaser, and A. Wismuller, "Computer-aided diagnosis in phase contrast imaging X-ray computed tomography for quantitative characterization of ex vivo human patellar cartilage," *IEEE Trans Biomed Eng*, vol. 60, no. 10, pp. 2896-903, Oct 2013, doi: 10.1109/TBME.2013.2266325.
- [21] T. Torheim *et al.*, "Classification of dynamic contrast enhanced MR images of cervical cancers using texture analysis and support vector machines," *IEEE Trans Med Imaging*, vol. 33, no. 8, pp. 1648-1656, Aug 2014, doi: 10.1109/TMI.2014.2321024.

- [22] P. Nguyen *et al.*, "Grey scale texture analysis of endobronchial ultrasound mini probe images for prediction of benign or malignant aetiology," *Respirology*, vol. 20, no. 6, pp. 960-966, Aug 2015, doi: 10.1111/resp.12577.
- [23] M. Pietikäinen and T. Ojala, "Texture analysis in industrial applications," in *Image Technology*: Springer, 1996, pp. 337-359.
- [24] J.-W. Chan, N. Laporte, and R. Defries, "Texture classification of logged forests in tropical Africa using machine-learning algorithms," *International Journal of Remote Sensing*, vol. 24, no. 6, pp. 1401-1407, 2003.
- [25] M. A. Akhloufi, X. Maldague, and W. B. Larbi, "A new color-texture approach for industrial products inspection," *Journal of multimedia*, vol. 3, no. 3, pp. 44-50, 2008.
- [26] M. P. Ferreira, F. H. Wagner, L. E. O. C. Aragão, Y. E. Shimabukuro, and C. R. de Souza Filho, "Tree species classification in tropical forests using visible to shortwave infrared WorldView-3 images and texture analysis," *ISPRS Journal of Photogrammetry and Remote Sensing*, vol. 149, pp. 119-131, 2019, doi: <https://doi.org/10.1016/j.isprsjprs.2019.01.019>.
- [27] J. S. Weszka and A. Rosenfeld, "An application of texture analysis to materials inspection," *Pattern Recognition*, vol. 8, no. 4, pp. 195-200, 1976, doi: [https://doi.org/10.1016/0031-3203\(76\)90039-X](https://doi.org/10.1016/0031-3203(76)90039-X).
- [28] E. Hayman, B. Caputo, M. Fritz, and J.-O. Eklundh, "On the significance of real-world conditions for material classification," in *European conference on computer vision*, 2004: Springer, pp. 253-266.
- [29] R. J. Gillies, P. E. Kinahan, and H. Hricak, "Radiomics: images are more than pictures, they are data," *Radiology*, vol. 278, no. 2, pp. 563-577, Feb 2016, doi: 10.1148/radiol.2015151169.
- [30] R. W. Conners and C. A. Harlow, "A theoretical comparison of texture algorithms," *IEEE Trans Pattern Anal Mach Intell*, vol. 2, no. 3, pp. 204-222, Mar 1980. [Online]. Available: <https://www.ncbi.nlm.nih.gov/pubmed/21868894>.
- [31] C. M. Wu, Y. C. Chen, and K. S. Hsieh, "Texture features for classification of ultrasonic liver images," *IEEE Trans Med Imaging*, vol. 11, no. 2, pp. 141-152, 1992, doi: 10.1109/42.141636.
- [32] W. Gomez, W. C. A. Pereira, and A. F. C. Infantosi, "Analysis of co-occurrence texture statistics as a function of gray-level quantization for classifying breast ultrasound," *IEEE Transactions on Medical Imaging*, vol. 31, no. 10, pp. 1889-1899, 2012.
- [33] W. L. Lee, Y. C. Chen, and K. S. Hsieh, "Ultrasonic liver tissues classification by fractal feature vector based on M-band wavelet transform," *IEEE Trans Med Imaging*, vol. 22, no. 3, pp. 382-392, Mar 2003, doi: 10.1109/TMI.2003.809593.

- [34] M.-C. Yang *et al.*, "Robust texture analysis using multi-resolution gray-scale invariant features for breast sonographic tumor diagnosis," *IEEE Transactions on Medical Imaging*, vol. 32, no. 12, pp. 2262-2273, 2013.
- [35] D. Y. Chong *et al.*, "Robustness-driven feature selection in classification of fibrotic interstitial lung disease patterns in computed tomography using 3D texture features," *IEEE Trans Med Imaging*, vol. 35, no. 1, pp. 144-157, Jan 2016, doi: 10.1109/TMI.2015.2459064.
- [36] X. Zang, R. Bascom, C. Gilbert, J. Toth, and W. Higgins, "Methods for 2-D and 3-D endobronchial ultrasound image segmentation," *IEEE Transactions on Biomedical Engineering*, vol. 63, no. 7, pp. 1426-1439, 2015.
- [37] A. Ortiz, J. M. Gorriz, J. Ramirez, D. Salas-Gonzalez, and J. M. Llamas-Elvira, "Two fully-unsupervised methods for MR brain image segmentation using SOM-based strategies," *Appl Soft Comput*, vol. 13, no. 5, pp. 2668-2682, May 2013, doi: 10.1016/j.asoc.2012.11.020.
- [38] C. Militello *et al.*, "Gamma Knife treatment planning: MR brain tumor segmentation and volume measurement based on unsupervised Fuzzy C-Means clustering," *International Journal of Imaging Systems and Technology*, vol. 25, no. 3, pp. 213-225, 2015.
- [39] B. Khomkham, A. Wattanathum, and R. Lipikorn, "Peripheral pulmonary lesion classification from endobronchial ultrasonography images using weight-sum of upper and lower GLCM feature," in *2017 7th IEEE International Conference on System Engineering and Technology (ICSET)*, 2017: IEEE, pp. 157-161.
- [40] L. Rundo *et al.*, "A novel framework for MR image segmentation and quantification by using MedGA," *Comput Meth Prog Bio*, vol. 176, pp. 159-172, Jul 2019, doi: 10.1016/j.cmpb.2019.04.016.
- [41] H. T. Xie, D. B. Yang, N. N. Sun, Z. N. Chen, and Y. D. Zhang, "Automated pulmonary nodule detection in CT images using deep convolutional neural networks," *Pattern Recognition*, vol. 85, pp. 109-119, Jan 2019, doi: 10.1016/j.patcog.2018.07.031.
- [42] C. Han *et al.*, "Synthesizing Diverse lung nodules wherever massively: 3D multi-conditional GAN-based CT image augmentation for object detection," in *2019 International Conference on 3D Vision (3DV)*, 16-19 Sept. 2019, pp. 729-737, doi: 10.1109/3DV.2019.00085.
- [43] Y. Liu, P. Hao, P. Zhang, X. Xu, J. Wu, and W. Chen, "Dense convolutional binary-tree networks for lung nodule classification," *IEEE Access*, vol. 6, pp. 49080-49088, 2018, doi: 10.1109/ACCESS.2018.2865544.
- [44] M. Z. Alom *et al.*, "A state-of-the-art survey on deep learning theory and architectures," *Electronics*, vol. 8, no. 3, p. 292, 2019.
- [45] W. Suraworachet, R. Lipikorn, and A. Wattanathum, "Pulmonary lesion boundary detection from an endobronchial ultrasonogram using polar sector maximum intensity," *International*

- Journal of Electronics and Electrical Engineering*, pp. 185-188, 2016, doi: 10.18178/ijeec.4.2.185-188.
- [46] B. Khomkham, "PULMONARY LESION TEXTURE CLASSIFICATION FROM ENDOBRONCHIAL ULTRASONOGRAPHY USING TEXTURE ANALYSIS," Master, Chulalongkorn University, 2017.
- [47] J. Yang and V. Honavar, "Feature subset selection using a genetic algorithm," in *Feature extraction, construction and selection*: Springer, 1998, pp. 117-136.
- [48] D. E. Goldberg, *Genetic Algorithms in Search, Optimization and Machine Learning*. Reading, MA: Addison-Wesley, 1989.
- [49] S. N. Sivanandam and S. N. Deepa, *Introduction to Genetic Algorithms*, Springer-Verlag Berlin Heidelberg, 2008
- [50] S. Oreski and G. Oreski, "Genetic algorithm-based heuristic for feature selection in credit risk assessment," *Expert Syst Appl*, vol. 41, no. 4, pp. 2052-2064, Mar 2014, doi: 10.1016/j.eswa.2013.09.004.
- [51] N. Suguna and K. Thanushkodi, "An improved k-nearest neighbor classification using genetic algorithm," *International Journal of Computer Science Issues*, vol. 7, no. 2, pp. 18-21, 2010.
- [52] T. V. Bandos, L. Bruzzone, and G. Camps-Valls, "Classification of hyperspectral images with regularized linear discriminant analysis," *IEEE Transactions on Geoscience and Remote Sensing*, vol. 47, no. 3, pp. 862-873, 2009.
- [53] M. Pal and G. M. Foody, "Feature selection for classification of hyperspectral data by SVM," *IEEE Transactions on Geoscience and Remote Sensing*, vol. 48, no. 5, pp. 2297-2307, 2010, doi: 10.1109/TGRS.2009.2039484.
- [54] J. Arunadevi, S. Ramya, and M. R. Raja, "A study of classification algorithms using Rapidminer," *International Journal of Pure and Applied Mathematics*, vol. 119, no. 12, pp. 15977-15988, 2018.
- [55] T. Fawcett, "An introduction to ROC analysis," *Pattern recognition letters*, vol. 27, no. 8, pp. 861-874, 2006.
- [56] U. Scheipers, C. Perrey, S. Siebers, C. Hansen, and H. Ermert, "A tutorial on the use of ROC analysis for computer-aided diagnostic systems," *Ultrasonic imaging*, vol. 27, no. 3, pp. 181-198, 2005.

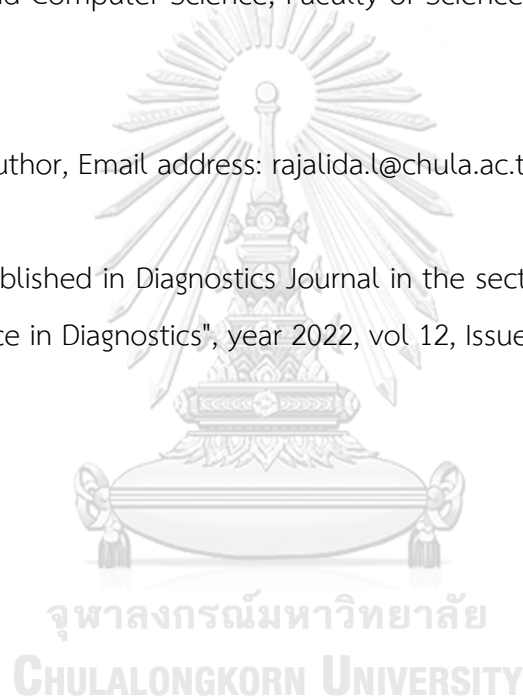
CHAPTER 4
PULMONARY LESION CLASSIFICATION FRAMEWORK USING THE
WEIGHTED ENSEMBLE CLASSIFICATION WITH RANDOM FOREST AND
CNN MODELS FOR EBUS IMAGES

Banphatree Khomkham and Rajalida Lipikorn*

Machine Intelligence and Multimedia Information Technology Laboratory, Department of Mathematics and Computer Science, Faculty of Science, Chulalongkorn University, Bangkok, Thailand

* Corresponding author, Email address: rajalida.l@chula.ac.th

This paper was published in *Diagnostics Journal* in the section "Machine Learning and Artificial Intelligence in Diagnostics", year 2022, vol 12, Issue 7, page 1552.



Received: 22 April 2022

Revised: 18 June 2022

Accepted: 24 June 2022

Published: 26 June 2022

ABSTRACT

Lung cancer is a deadly disease with a high mortality rate. Endobronchial ultrasonography (EBUS) is one of the methods for detecting pulmonary lesions. Computer-aided diagnosis of pulmonary lesions from images can help radiologists to classify lesions; however, most of the existing methods need a large volume of data to give good results. Thus, this paper proposes a novel pulmonary lesion classification framework for EBUS images that works well with small datasets. The proposed framework integrates the statistical results from three classification models using the weighted ensemble classification. The three classification models include the radiomics feature and patient data-based model, the single-image-based model, and the multi-patch-based model. The radiomics features are combined with the patient data to be used as input data for the random forest, whereas the EBUS images are used as input data to the other two CNN models. The performance of the proposed framework was evaluated on a set of 200 EBUS images consisting of 124 malignant lesions and 76 benign lesions. The experimental results show that the accuracy, sensitivity, specificity, positive predictive value, negative predictive value, and area under the curve are 95.00%, 100%, 86.67%, 92.59%, 100%, and 93.33%, respectively. This framework can significantly improve the pulmonary lesion classification.

KEYWORDS: pulmonary lesion, endobronchial ultrasonography images (EBUS), convolutional neural network (CNN), radiomics features, random forest, gray-level co-occurrence matrix (GLCM), weighted ensemble

4.1 Introduction

Cancer has been regarded as the leading cause of death among the world's population from past to present, and its prevalence is expected to rise steadily. Among many types of common cancers, lung cancer is the leading cause of death, followed by colorectal, liver, stomach, and female breast cancers. According to the International Agency for Research on Cancer, there were 2.2 million new cases of lung cancer diagnosed and 1.8 million deaths globally in 2020 [1]. The majority of lung cancer patients do not show symptoms until the disease has advanced, but some early lung cancer patients may show the symptoms; therefore, early diagnosis can lower the mortality rate significantly [2]. Furthermore, lung cancer can be cured, and treatment is more effective if it is detected early [3,4]. In general, there are many techniques for diagnosis and staging of lung cancer such as computed tomography (CT), positron emission tomography—computed tomography (PET-CT), magnetic resonance imaging (MRI), and EBUS [5–7]. EBUS has become popular in recent years since this technique utilizes no radiation and scans in real time. It is the most recent screening technology for obtaining small wounds with minimal pain [8]. Although EBUS is a good way to detect lung cancer early, its performance is limited by tissue superposition, which can result in false-negative diagnoses [9].

In clinical research, many researchers attempt to find criteria to distinguish pulmonary lesions in EBUS images by using both retrospective and prospective methods [10–13]. According to previous research [14], the characteristics of malignant lesions in EBUS images have a heterogeneous pattern, a short axis, presence of coagulation necrosis sign, round shape, distinct margin, and absence of central hilar structure, while the characteristics of benign lesions in EBUS images show the presence of calcification, nodal conglomeration, and echo intensity. As a result, in visual tasks, precise and reliable EBUS interpretation and lung cancer diagnosis are extremely challenging and also depend on the skills and experiences of radiologists. Therefore, several computer-aided diagnosis (CAD) methods have been proposed to address this problem.

Morikawa et al. [15] studied 30 malignant and 22 benign EBUS images from 60 patients who were subjected to a bronchoscopy using histogram-based quantitative

evaluation of EBUS images. The regions of interest (ROIs) inside EBUS images were suitably selected by experimenting with a phantom model submerged in water to extract six histogram features. The extracted features of EBUS images were distinguished by using Mann–Whitney U tests.

Alici et al. [16] processed 1051 lymph nodes from 532 patients by using the sonographic features such as grayscale, echogenicity, shape, size, margin, presence of necrosis, presence of calcification, and absence of central hilar structure via EBUS images. Decision tree analysis was applied to discriminate lymph nodes between benign and malignant.

Khomkham and Lipikorn [17] proposed two robust features that were extended from a gray-level co-occurrence matrix (GLCM) as well as a technique for lung cancer classification utilizing a genetic algorithm and support vector machines (SVM). The classification performance with accuracy, sensitivity, specificity, and precision is 86.52%, 87.27%, 85.29%, and 90.57%, respectively.

Gómez et al. [18] studied the performance of 22 co-occurrence statistics in conjunction with six gray-scale quantization levels to identify breast lesions on ultrasound (BUS) images. The 436 BUS images were utilized in this study; the number of carcinoma lesions was 217 and the number of benign lesions was 219. The best area under the curve obtained from using 32 gray levels and 109 features was 0.81.

Radiomics analysis is also widely used in cancer diagnosis [15–18]. The concept of radiomics analysis is to extract a massive number of quantitative features from medical images by using shape features, first order features, second order features, or higher order features. In recent years, deep learning (DL) methods have been used tremendously in computer vision aided by advances in computation and very large amounts of data. In comparison to traditional machine learning, deep learning can accurately detect appropriate features for particular classification tasks and possibly clarify feature selection problems without the need for complicated image processing pipelines and pattern recognition procedures. As a superb method in DL technology, convolutional neural network (CNN) has been significantly improved in image classification and object detection, including medical imaging and it is now one of the

dominant methods. CNN has been applied to medical images to solve many different problems.

Jia et al. [19] presented a novel framework for properly classifying cervical cells based on the strong feature CNN–support vector machine (SVM) model. The technique was developed for merging the strong features recovered by GLCM and Gabor with abstract features acquired from CNN’s hidden layers. Their method outperformed state-of-the-art models with 99.3 percent of accuracy.

Tan et al. [20] proposed a modified CNN-based 3D-GLCM to classify polyps in colonography. This model could handle a small number of datasets by using the advantage of GLCM features. The experimental results show that CNN learning from GLCMs out-performs CNN on raw CT images in terms of classification performance. The model achieves up to 91 percent accuracy by using two-fold cross-validation.

Islam et al. [21] created a deep learning approach consisting of the combination of CNN and long short-term memory (LSTM) to autonomously diagnose COVID-19 via X-ray images. The CNN was utilized for deep feature extraction, while LSTM was used for standard feature extraction and COVID-19 diagnosis. The experimental results reveal that the suggested method obtained an accuracy of 99.4 percent.

Li et al. [22] used chest X-ray (CXR) images to assess the predictive performance of DL models in the recognition and classification of pneumonia. In the pooling step, they utilized bivariate linear mixed models. The results demonstrate that DL performed well in differentiating bacterial from viral pneumonia and in categorizing pneumonia from normal CXR radiographs.

Zhang et al. [23] developed a ResNet model for medical picture classification in smart medicine by replacing global average pooling with adaptive dropout. The results of the experiments on a GPU cluster indicate that the provided model delivered excellent recognition performance without a significant loss in efficiency.

Cai et al. [24] developed a mask region–convolutional neural network (Mask R–CNN) and ray-casting volume rendering algorithm-based detection and segmentation techniques for lung nodule 3D visualization diagnosis. Mask R–CNN of weighted loss achieved sensitivities of 88.1 percent and 88.7 percent, respectively.

Wang et al. [25] presented a new multiscale rotation-invariant convolutional neural network (MRCNN) model for identifying different kinds of lung tissue using high-resolution computed tomography. The suggested technique outperformed the most recent findings on a public interstitial lung disease database.

Anthimopoulos et al. [26] proposed to use a deep CNN to categorize patch-based CT image into seven groups, containing six distinct interstitial lung disease patterns and healthy tissue. A new network architecture was created to capture the low-level textural characteristics of lung tissue. According to the experiments, the categorization performance was around 85.5 percent.

In 2019, Chen et al. [27] proposed the CAD system for differentiating lung lesions via EBUS images using CNN. Because the dataset was small, data augmentation was performed by flipping and rotating images. Then the fine-tuned CaffeNet-SVM was used to differentiate lung lesions. The experimental results revealed that the proposed system to achieve up to 85.4 percent accuracy.

In 2021, Lei et al. [28] proposed a low-dose CT image denoising method for improved performance of lung nodule classification. Because scans have substantial noise, they have significant influence on lung nodule classification. The proposed method enables cooperative training of image denoising and lung nodule classification by utilizing self-supervised loss and cross-entropy loss. According to the experiments, the simultaneous training of image denoising and lung nodule classification increases the performance significantly.

Lei et al. [29] proposed a novel method for analyzing shape nodule with a CNN using soft activation mapping. Soft activation mapping captures more fine-grained and discrete attention regions to locate the low-grade malignant nodule. The results of the experiments on the LIDC-IDRI dataset revealed that the proposed method outperformed state-of-the-art models in terms of false positive rate.

Ensemble methods are techniques for developing multiple models and then combining them to produce better results. Moreover, when compared to a single model, ensemble approaches often produce more accurate results. Recently, an ensemble method has been reported in a variety of fields. The ensemble method has been applied to medical images to solve many different problems. Guo et al. [30]

proposed an ensemble learning method for COVID-19 diagnosis via CT obtained by using ordinal regression. This model could enhance classification accuracy by learning both intraclass and interclass links between phases. The experimental results revealed that as modified ResNet-18 was utilized as the backbone; accuracy rose by 22% when compared to standard approaches.

However, most of the existing techniques need large datasets to yield satisfactory results. Thus, this paper proposes a novel pulmonary lesion classification framework that does not need a large training dataset by combining radiomics features and patient data with standard features that are extracted from EBUS images as input data, then using random forest, CNN, and weighted ensemble to classify pulmonary lesions.

The structure of this paper is as follows: Section 4.2 describes the details of the materials; Section 4.3 explains the proposed framework; the results and discussion are summarized in Section 4.4; and Section 4.5 provides the conclusion.

4.2 Materials

The data used for evaluation of the proposed framework consist of both EBUS images and patient data. The EBUS images were obtained by skilled radiologists from Phramongkutklao Hospital, Bangkok, Thailand, between November 2011 and May 2016. The EBUS images were obtained using an endoscopic ultrasound system (EU-ME1; Olympus) and a 20 MHz miniature radial probe (UM-S20-17S; Olympus). The probe provides a 360-degree panoramic ultrasonic view of the lesion. The radiologists collected 200 EBUS images from 200 patients. There are 124 malignant lesions and 76 benign lesions. The image format is an 8-bit RGB image. The size of each image was cropped to 776×776 pixels. Examples of different pulmonary lesion patterns in EBUS images are shown in Figure 4.1.

For patient data, both numerical and categorical data that were used consist of gender (male, female), smoking history (smoker, no smoker, and ex-smoker), age (between 17 and 86), and lesion size (less than 3 cm, more than or equal to 3 cm) as shown in Table 4.1.

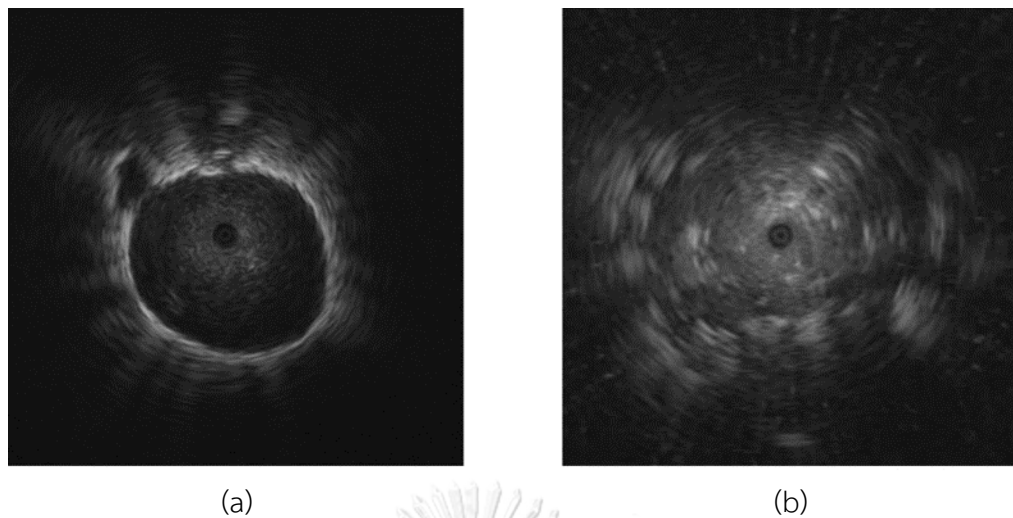


Figure 4.1 Examples of different pulmonary lesion patterns in EBUS images: (a) benign lesion; (b) malignant lesion (benign and malignant lesions were confirmed after core needle biopsy).

Table 4.1 Clinical details of the patients.

	Malignant	Benign
Number of patients	124 (74 male,50 female)	76 (29 male, 47 female)
Age (Mean±SD)	64.32± 13.21	57.63 ±15.51
Lesion size	≥3cm (75), <3cm (49)	≥3cm (38), <3cm (38)
Smoking History	non-smoking (52), smoking (35), ex-smoking (37)	non-smoking (29), smoking (27), ex-smoking (20)

4.3 Methods

The proposed pulmonary lesion classification framework is shown in Figure 4.2. The framework is based on the integration of three modified machine learning models and the weighted ensemble classification. The three modified machine learning models are the radiomics feature and patient data-based model, the single image-based model, and the multi-patch-based model.

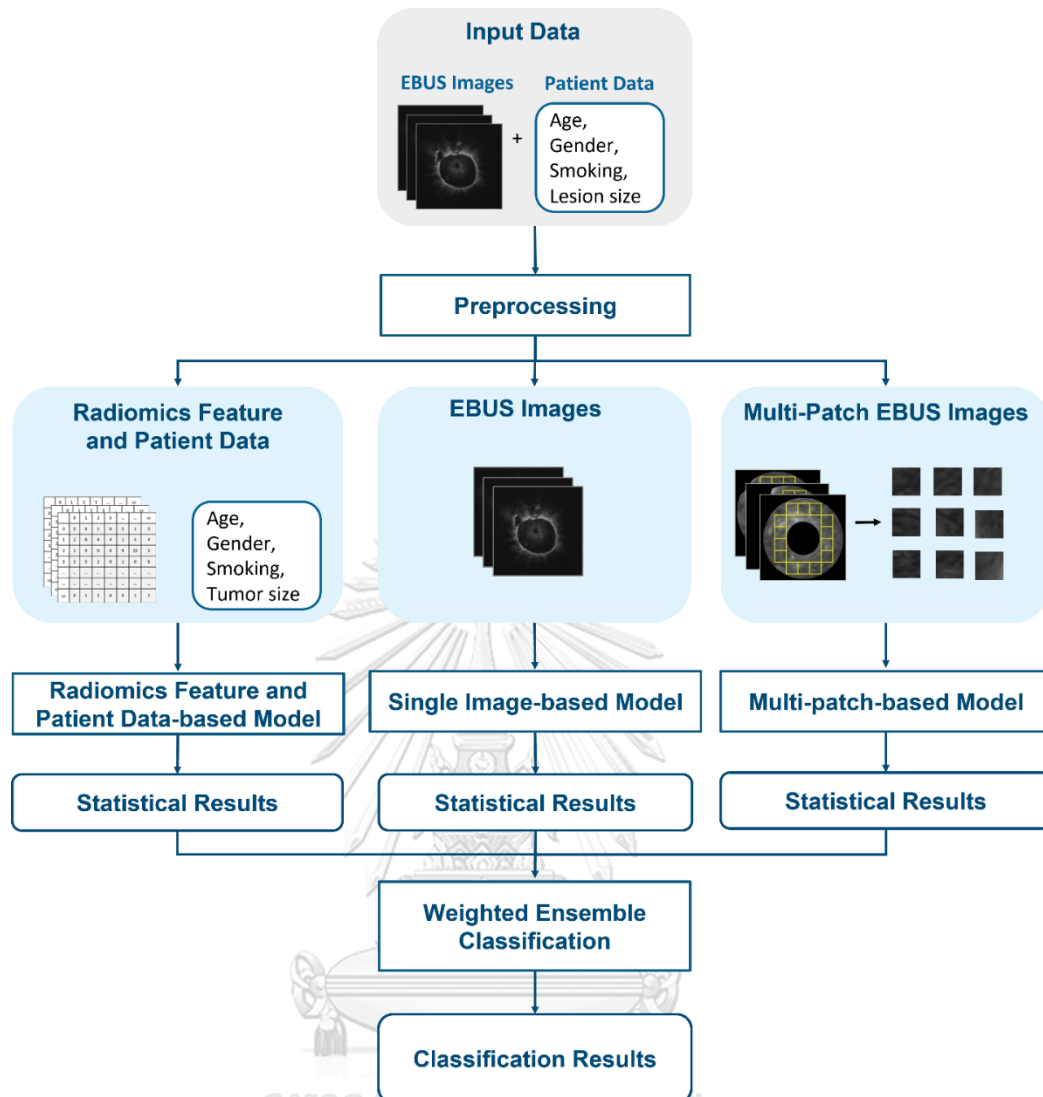


Figure 4.2 The framework of the proposed pulmonary lesion classification system.

4.3.1 Preprocessing

The preprocessing step consists of class balancing, mask generation, feature extraction, and window of interest (WOI) selection. The class balancing was performed to generate more data and balance the amount of training data for the models since our dataset contains only 200 EBUS images. Then the EBUS images were converted to grayscale images to be used in mask generation and the radiomics feature and patient data-based model, while the original RGB EBUS images were used in the single image-based model and the multi-patch-based model. Mask generation was performed to define the region of lesion for the single image-based model and the multi-patch-

based model. The window of interest selection was performed to divide the region of lesion into small patches which were used for the multi-patch-based model.

4.3.1.1 Class Balancing

Because the dataset is too small and there are more malignant images than benign images, image augmentation, which is an effective way to increase the amount of data without having to obtain new images, was performed to balance the data. The augmentation methods used in this paper are rotation, vertical flipping, and horizontal flipping to preserve the main characteristics of the images. The images were rotated by 90 and 180 degrees, and they were also flipped vertically and horizontally, as shown in Figure 4.3.

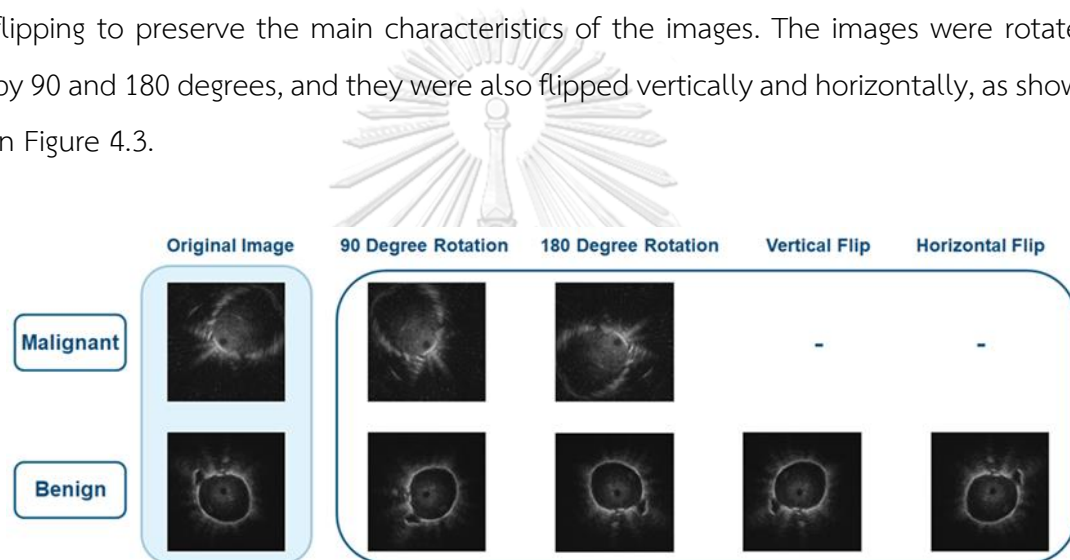


Figure 4.3 Data augmentation for malignant and benign images.

Data augmentation combines both malignant strategy and benign strategy [26] to balance data in both training classes; therefore, the images in malignant class were rotated but were not flipped because there were more malignant images than benign images. From 200 EBUS images, 160 images (80% of the dataset) were used as training data and 40 images (20% of the dataset) were used as test data. After augmentation, the total number of training data for both classes increased from 160 to 602. The number of augmented malignant and benign images is shown in Table 4.2.

Table 4.2 Distribution of EBUS images after class balancing.

	Malignant	Benign	All
Original EBUS image data	99	61	160
Augmented image data	198	244	442
Total of training image data	297	305	602

4.3.1.2 Mask Generation

In this step, the mask that was used to represent the region of lesion within the boundary in each EBUS image was generated. The mask generation consists of two main parts: image enhancement and boundary detection. In the medical field, many techniques have been introduced to enhance image quality [31,32]. Contrast stretching (CS) [33] is one of the enhancement techniques that is used to deal with adjusting contrast and improving image quality in the region of interest. By using CS, the bright components can be made brighter, while the dark background can be made darker. CS operation on an image is shown in Equation (1):

$$\bar{I}(x,y) = \begin{cases} 0, & I(x,y) < L \\ I(x,y)^\gamma, & L \leq I(x,y) \leq H \\ 1, & I(x,y) > H \end{cases} \quad (1)$$

where $I(x,y)$ is the original image, (x,y) are the coordinates of a pixel, $\bar{I}(x,y)$ is the enhanced image, L is the low threshold intensity, H is the high threshold intensity, and γ is a constant value.

After enhancing the images, the next step is boundary detection. There are many boundary detection techniques [34–37] that can be applied, and the technique called ray tracing is the technique that was used to detect the lesion boundary in this paper [37]. Once the boundary was detected, the mask of the original image was generated by as-signing 1 to the area inside the boundary and 0 to the area outside the boundary. Figure 4.4(b) shows the mask of the original image in Figure 4.4a. Figure

4.4(c) shows the region of lesion that can be obtained by performing AND operation between Figure 4.4(a), (b).

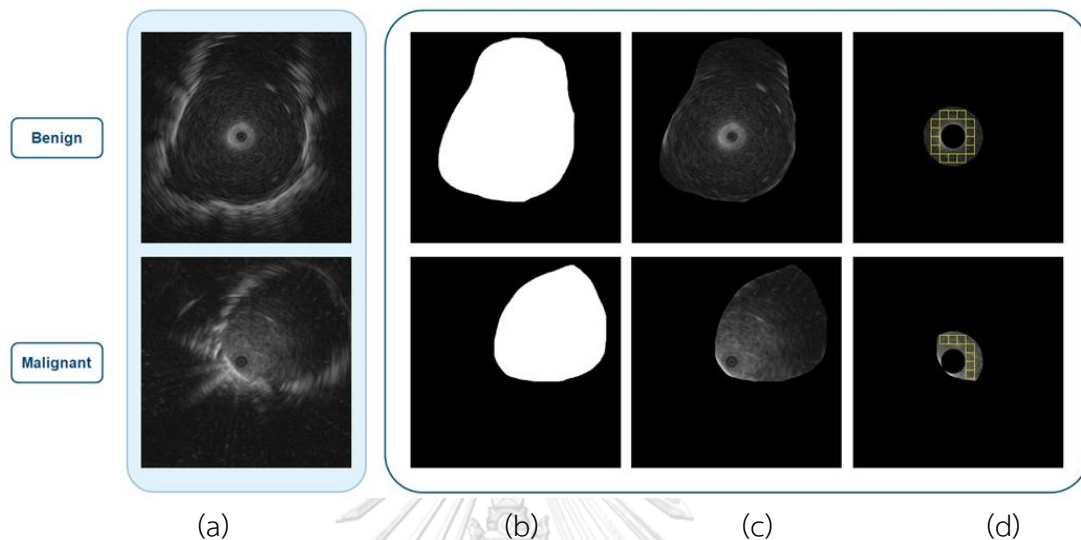


Figure 4.4 Results from the preprocessing step: (a) Original images; (b) mask images; (c) regions of interest; (d) WOIs in the intersection area of the region of interest and the ring

4.3.1.3 Feature Extraction

There are several other important features that can be extracted from EBUS images and can be utilized for lesion classification and texture analysis. Feature extraction is performed to improve the performance of the classifier by searching for the most condensed and informative set of features. Radiomics features are widely used in many fields of pattern recognition, computer vision, and image classification. In this paper, the radiomics features were extracted from the area of lesion inside the boundary, as shown in Figure 4.4(c). The radiomics features, which consist of six classes: shape-based 2D (9 features), GLCM (24 features), gray-level dependence matrix (GLDM) (14 features), gray-level run length matrix (GLRLM) (16 features), gray level size zone matrix (GLSZM) (16 features), and neighboring gray tone difference matrix (NGTDM) (5 features), were extracted using the pyradiomics package [38]. Another GLCM feature known as the adaptive weighted-sum of the upper and lower triangular GLCM or AWS is also included in the radiomics features [17]. This feature is effective at determining

heterogeneity, which is one of the most important characteristics of malignancy. Besides radiomics features, four features were extracted from patient data: gender, smoking history, age, and lesion size. The total number of features is 89 features. All features used in this paper and their correlations are shown using the correlation heatmap [39] in Figure 4.5.

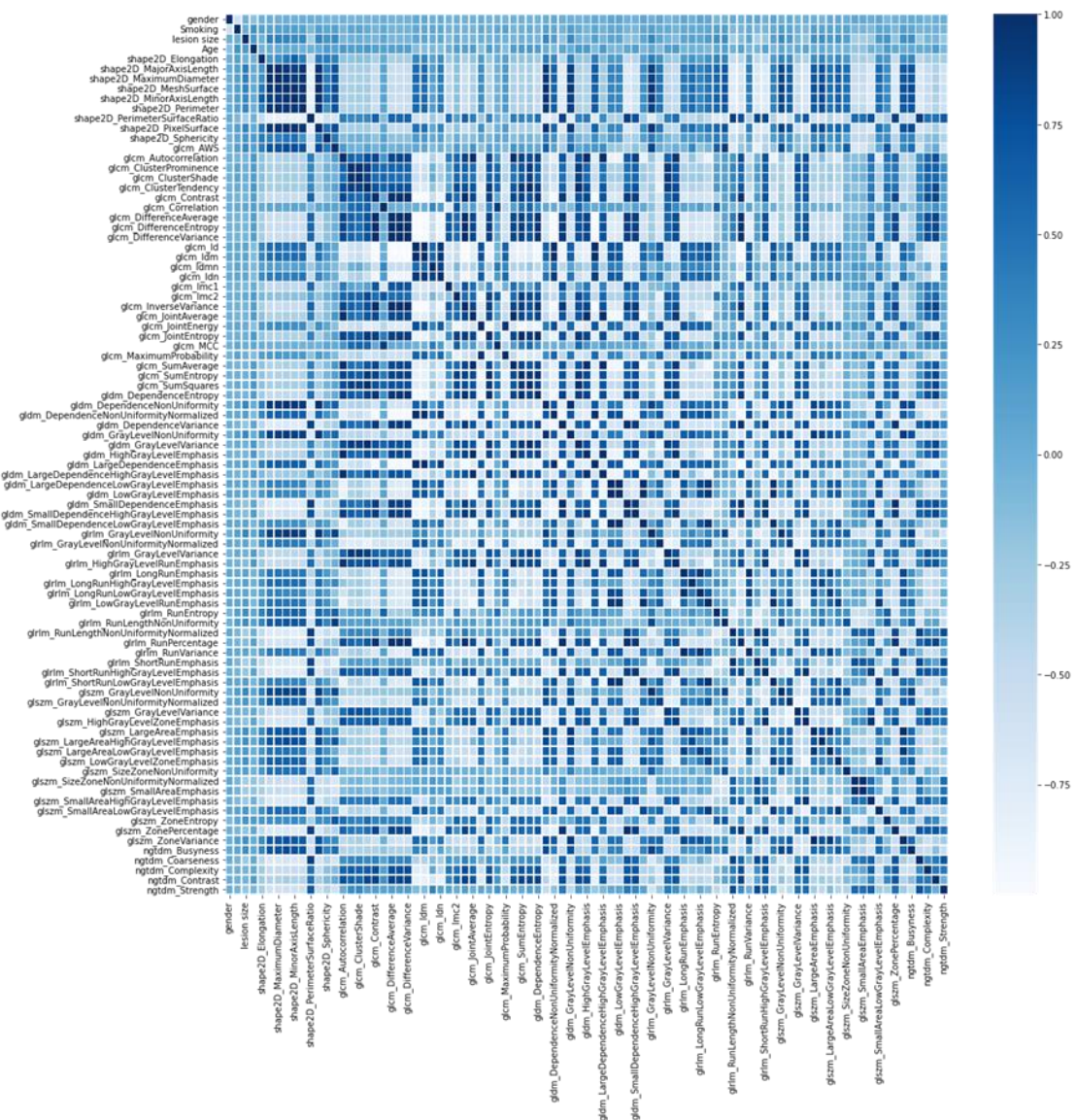


Figure 4.5 Heat map of Pearson correlation coefficient matrix for all features.

4.3.1.4 WOI Selection

The last step of preprocessing is WOI selection which prepares the input data for the multi-patch-based model. The WOI selection divides a lesion into small patches or windows. The study by Morikawa et al. [15] found that the most suitable region of lesion is the ring between 2 mm to 5 mm from the probe, thus the patches were selected from this ring. The size of the patch was derived from the size of the biggest square window that can fit within the ring which is 32×32 pixels. The patches in each ring are all the windows that can be tiled inside the ring area as shown in Figure 4.4 (d).

4.3.2 The Proposed Framework

The proposed framework consists of three machine learning models that were used to calculate the probability of being benign or malignant. The first model is based on radiomics features and patient data, the second model is based on the original EBUS images, and the third model is based on multiple patches of lesion.

4.3.2.1 Radiomics Feature and Patient Data-Based Model

The first model consists of feature selection and classification as shown in Figure 4.6. Feature selection was performed to reduce the number of features that are redundant and irrelevant. Mutual information (MI) criterion [40] which is one of the feature selection techniques was used to select relevant features from radiomics features and patient data. MI between feature and target class is a non-negative value that measures dependency. It is equal to zero if and only if two variables are independent; higher value means higher dependency.

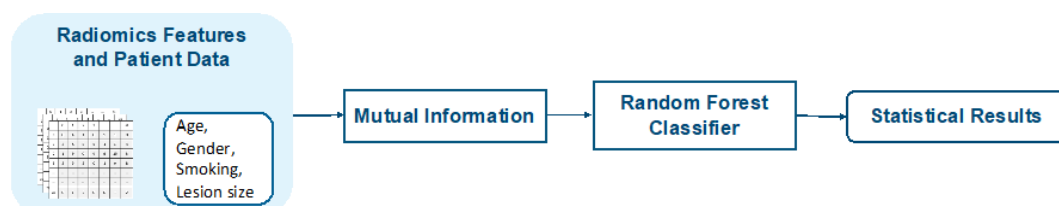


Figure 4.6 Block diagram of the radiomics feature and patient data-based model.

A subset of selected features that were obtained after applying mutual information criterion were used as input to the random forest classifier (RF) [41]. RF is a supervised machine learning classifier that is composed of as many decision trees on different samples as possible and combines the output from all the trees. RF can decrease overfitting problems in decision trees, as well as variation, and hence improve accuracy. RF is also one of a few classifiers that can handle both categorical and numerical features. RF is trained on a subset of selected features that contains both patient data and radiomics features. The output is the probability of being benign or malignant, P_1 .

4.3.2.2 Single Image-Based Model

The second model uses the original EBUS images as input data for the fine-tuned dense convolutional network 169 (DenseNet) [42]. DenseNet feature extractor was used to extract both local and global characteristics from an image. These local characteristics focus on the patterns of texture; i.e., homogeneity, heterogeneity, hyperechoic dot, hyperechoic arc, anechoic area, and linear air bronchogram while global characteristics focus on shape, size, and patterns of the texture of the whole lesion. DenseNet 169 architecture connects all layers densely. Each layer receives input from the preceding layers and forwards its output to the subsequent layers via its feature map. Its goal is to remove the redundant layer. Each layer inherits collective knowledge from the layers before it. Consequently, the classification layer receives data from all of the preceding layers as input data. DenseNet169 can produce excellent results, but fine-tuning their hyper parameters requires expert knowledge, a large dataset, and a significant amount of time, thus transfer learning [43] is used to solve such problems. DenseNet 169 can reuse the previously trained model. The idea behind transfer learning is to use a complicated and effectively pre-trained model, such as ImageNet, and then apply the learned knowledge to a new problem with a small dataset (EBUS images for this paper). DenseNet 169 is trained from ImageNet [44] and the weights from the first convolutional layer in block 1 to the last convolutional layer in block 8 are frozen. The classification layer was trained by EBUS images, separately.

The output layer of the fine-tuned DenseNet 169 for the single image-based model returned the probability of being benign or malignant, P_2 . The architecture of the fine-tuned DenseNet 169 for the single image-based model is shown in Figure 4.7 and the hyper-parameters of the model are shown in Table 4.3.

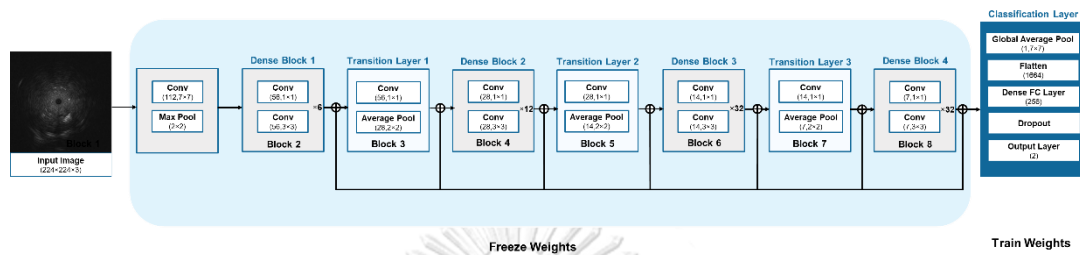


Figure 4.7 The architecture of the fine-tuned DenseNet 169 for the single image-based model.

Table 4.3 The hyper-parameters of DenseNet 169 architecture.

Hyper-parameter	Value
Optimizer	Stochastic Gradient Descent
Learning rate	0.0001
Loss function	Cross-entropy
Batch size	32

4.3.2.3 Multi-Patch-Based Model

The third model is called the multi-patch-based model because it uses all patches of size 32×32 pixels from each image as input to the proposed CNN. Since the input of this model was the patch, the CNN feature extractor was used to extract only local characteristics. The proposed CNN architecture for multi-patch images is shown in Figure 4.8.

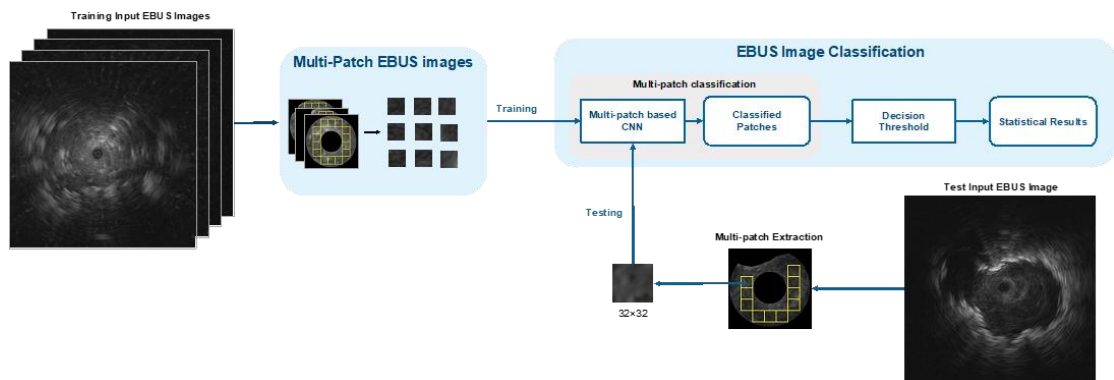


Figure 4.8 The architecture of the multi-patch-based model.

The architecture of the proposed CNN is shown in Figure 4.9. The input is convolved by a series of four convolutional layers. The size of kernels of these convolutional layers is set to 3×3 . The numbers of kernels of four convolutional layers are 8, 16, 32, and 64, respectively, as shown in Table 4.4. Every convolutional layer is followed by ReLU activation and Max pooling. The kernel size of Max pooling layers is set to 2×2 with no padding.

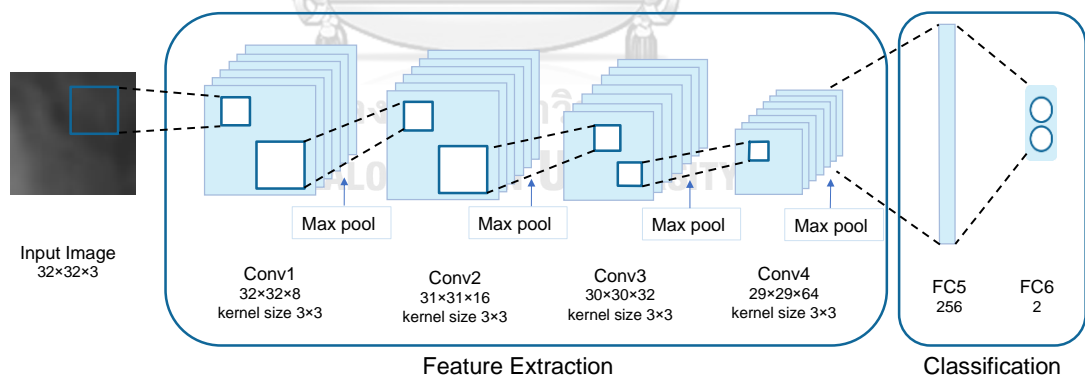


Figure 4.9 The architecture of the proposed CNN in the multi-patch-based model.

Table 4.4 The configuration of CNN for the multi-patch-based model.

Layer	Type	Kernel size	Stride	Output size
Data	Input			3×32×32
Conv1	Convolution	3×3	1	8×32×32
Conv2	Convolution	3×3	1	16×31×31
Conv3	Convolution	3×3	1	32×30×30
Conv4	Convolution	3×3	1	64×29×29
FC5	Fully connected			256×1×1
FC6	Fully connected			2×1×1

Every convolutional layer is followed by pooling layer. The ReLU activation function is not shown for brevity.

The batch size which defines the number of samples that are propagated through the network is set to 128. Dropout and batch normalization are also applied to prevent overfit-ting problems. The two-dimensional output is flattened and SoftMax activation is used to calculate the categorical probability distribution. The hyper-parameters of CNN architecture are shown in Table 4.5.

Table 4.5 The hyper-parameters of CNN architecture for the multi-patch-based model.

Hyper-parameter	Value
Optimizer	Adam
Learning rate	0.001
Loss function	Cross-entropy
Batch size	128

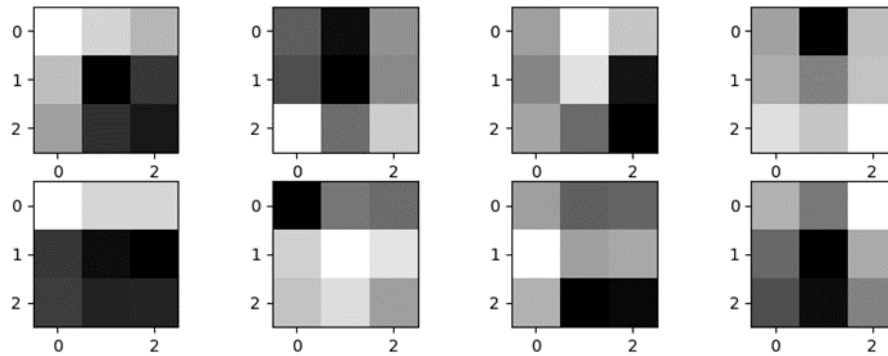


Figure 4.10 Weights learned by the first convolutional layer.

Figure 4.10 depicts how we visualize the learned features. Although there are no discernible structures, they are useful for classifying the texture of pulmonary lesions. Since each image contains the classification results of multiple patches, the classification result for each image can be obtained by using the decision threshold. The decision threshold is used to classify whether a lesion in an image is benign or malignant by calculating the probability of being malignant from the ratio of the patches that are classified as malignant to the total number of patches of an image as defined by Equation (2).

$$P_3(I) = \frac{n_M}{n_B + n_M} \quad (2)$$

where n_M is the number of malignant patches, n_B is the number of benign patches. If the probability is less than the decision threshold value, T , then a lesion is classified as benign; otherwise, malignant as defined by Equation (3).

$$Class(I) = \begin{cases} 1 & \text{if } P_3(I) > T \\ 0 & \text{otherwise} \end{cases} \quad (3)$$

where $P_3(I)$ is the probability of being malignant I . Class 0 represents benign, and class 1 represents malignant.

4.3.3 Weighted Ensemble Classification

The last step of the framework is to finally classify a lesion using the weighted ensemble classification [45] with the probability distributions from the three models as de-fined by Equation (4):

$$P(I) = w_1 P_1(I) + w_2 P_2(I) + w_3 P_3(I), \quad (4)$$

$$w_1 + w_2 + w_3 = 1, \quad (5)$$

where $P(I)$ is the probability of being malignant, w_1 , w_2 , and w_3 are the weight of each model with the sum of these three weights equal to 1. P_1 is the probability from the radiomics feature and patient data-based RF, P_2 is the probability from the single image-based CNN, and P_3 is the probability from the multi-patch-based CNN. If $P(I)$ is less than the cutoff value then a lesion is benign; otherwise, malignant. The optimal cutoff value is defined by the value that yields the highest accuracy during the training.

4.3.4 Performance Evaluation

The proposed pulmonary lesion classification framework is evaluated on the dataset that is randomly partitioned into two sets of 80:20. The training set consists of 80% of the data, while the test set consists of the remaining 20% of the data.

The performance is measured using six statistical indicators: accuracy (Acc) sensitivity (Sen), specificity (Spec), positive predictive value (PPV), negative predictive value (NPV), and area under the curve (AUC) as defined by Equations (6)–(10).

$$\text{Acc} = \frac{\text{correctly detected cases}}{\text{total cases}} \quad (6)$$

$$\text{Sen} = \frac{\text{correctly detected malignant cases}}{\text{total malignant cases}} \quad (7)$$

$$\text{Spec} = \frac{\text{correctly detected benign cases}}{\text{total benign cases}} \quad (8)$$

$$\text{PPV} = \frac{\text{correctly detected malignant cases}}{\text{detected malignant cases}} \quad (9)$$

$$\text{NPV} = \frac{\text{correctly detected benign cases}}{\text{detected benign cases}} \quad (10)$$

4.4 Experimental Results and Discussion

This section presents the experimental setup and the experimental results with discussion.

4.4.1 Experimental Setup

All the experiments were performed on a workstation (Intel (R) Core (TM) 3.00 GHz processor with 16 GB of RAM) and a NVIDIA GeForce GTX1650GPU. For preprocessing, the experiments were performed using MATLAB R2020b. For the classification, the experiments were implemented by python programming language with python libraries such as Keras, pandas, Scikit-learn, and NumPy.

4.4.2 Experimental Results

The results of EBUS image enhancement, feature selection for the radiomics feature and patient data-based model, and the classification results of the proposed framework are described in this section.

4.4.2.1 EBUS Image Enhancement

To improve the quality of all EBUS images, the parameter setting for CS includes L and H which were determined by sorting the intensity values of an image. From our dataset, the optimal values for L and H were at 1 percentile and 99 percentiles of intensity values. The enhanced images and their histograms are shown in Figure 4.11. After EBUS image enhancement was performed, more details of lesion components can be clearly seen. Figure 4.11(a) depicts the original image, while Figure 4.11(c)

depicts the enhanced image. The histograms of these two images show that the range of intensity values was widened after using CS.

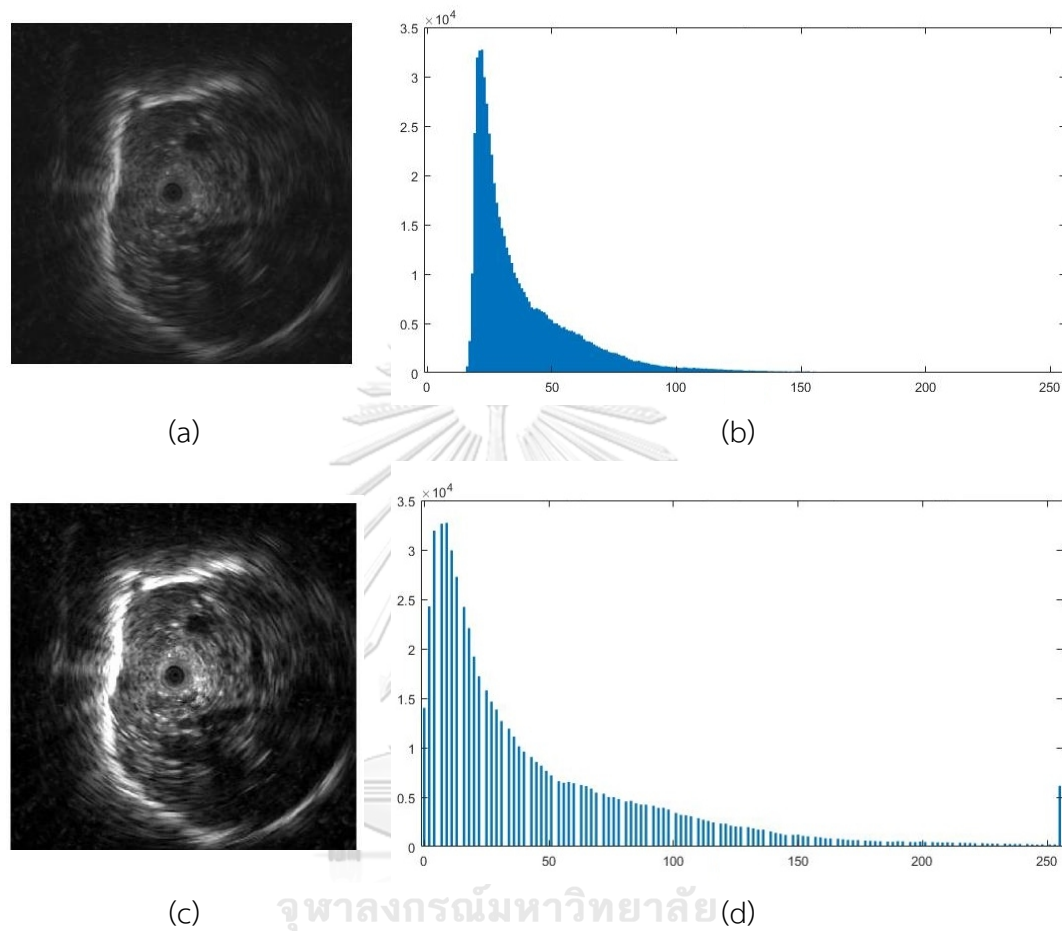


Figure 4.11 (a) The original EBUS image; (b) the histogram of (a); (c) the enhanced EBUS image; (d) the histogram of (c).

4.4.2.2 Feature Selection

Mutual information was performed on radiomics features and patient data to select only relevant features that are necessary for radiomics features and patient data-based model, and the most effective number of selected features was 57 out of 89 features. Figure 4.12 shows 57 features that were selected from both radiomics features and patient data with MI scores greater than zero.

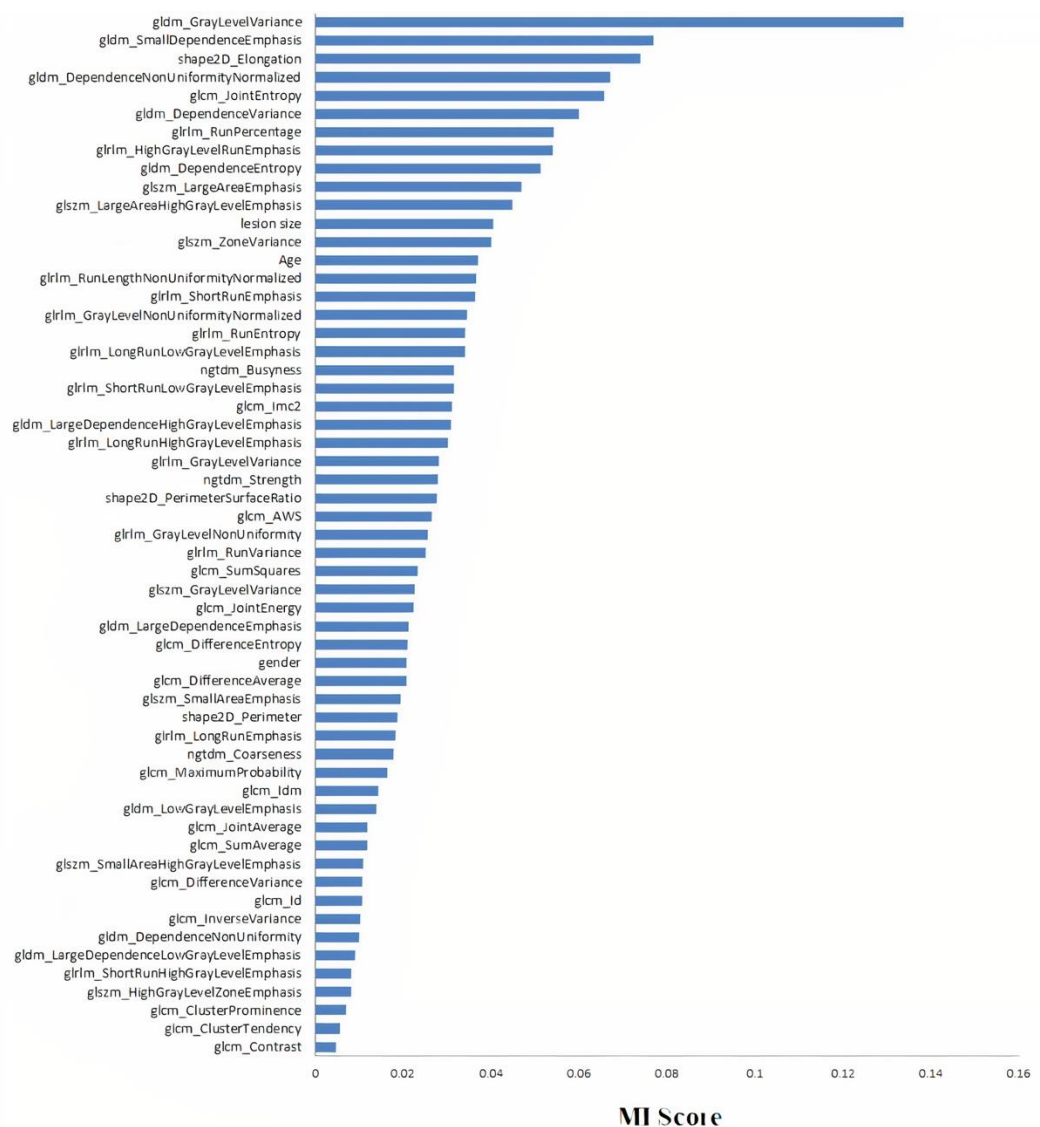


Figure 4.12 Feature selection of radiomics feature and patient data-based model.

4.4.2.3 Classification Performance

The performance of each model and the proposed classification framework were evaluated. For the radiomics feature and patient data-based model, the most suitable learning parameters were determined through the training using data from 200 patients who have both EBUS images and patient data. The RF classifier was performed on 57 features that were selected by MI. The forest's tree number was set to 1000, the Gini index was used as the split quality measure, and the minimum number of samples required to divide an internal node was set to two. Table 4.6 displays the RF performance. It can be seen that the RF performance can achieve up to 85% of

accuracy. The subset of relevant features consisting of three patient data and 54 out of 85 radiomics features were chosen. This indicates that radiomics features and patient data are important in the analysis of pulmonary lesions.

Figure 4.13(a) shows the confusion matrix of radiomics feature and patient data-based model. From the test set of 40 EBUS images, two lesions out of 25 malignant lesions were misclassified as benign, while four lesions out of 15 benign lesions were misclassified as malignant.

Table 4.6 The classification performance of different classification models.

	Acc	Sen	Spec	PPV	NPV	AUC
Radiomics feature and patient data-based model	85.00	92.00	73.33	85.19	84.62	0.8267
Single image-based model	75.00	88.00	53.33	75.86	72.72	0.7067
Multi-patch-based model	87.50	88.00	86.67	91.67	81.25	0.8733
Proposed framework	95.00	100.00	86.67	92.59	100.00	0.9333

The values in bold font indicate the best index values.

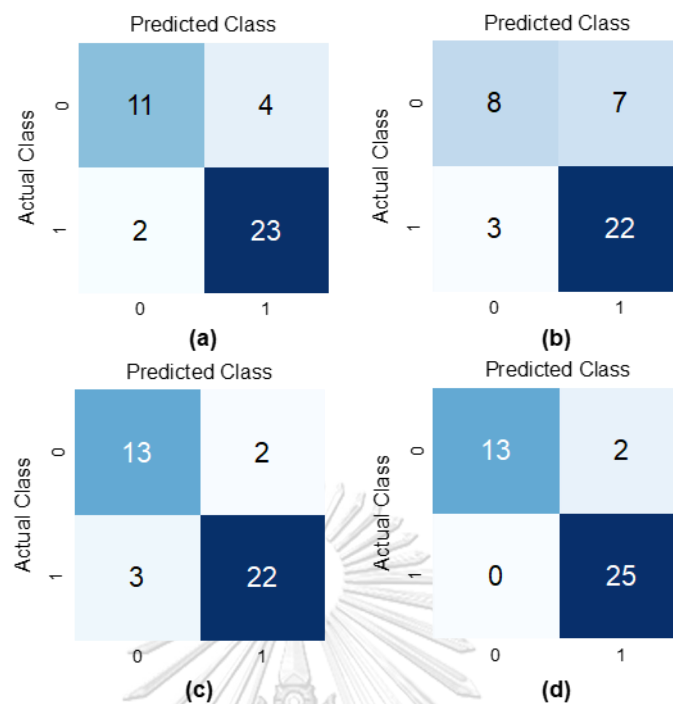


Figure 4.13 Confusion matrices:(a) the radiomics feature and patient data-based model; (b) the single image-based model; (c) the multi-patch-based model, and (d) the proposed framework.

Figure 4.14 depicts the misclassification results from the radiomics feature and patient data-based model. Figure 4.14(a) shows a malignant lesion that was misclassified as benign because the texture of the lesion is homogeneous with no echoic arc and echoic dot, whereas a benign lesion in Figure 4.14(b) was misclassified as malignant because its texture is heterogeneous, which is a common characteristic of malignant lesions, thus making it difficult to classify correctly.

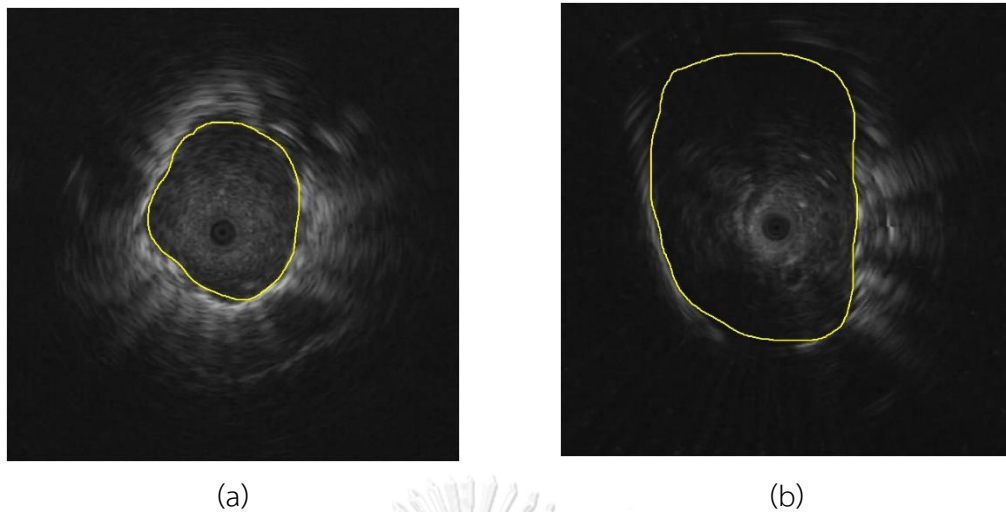


Figure 4.14 Misclassification of the radiomics feature and patient data-based model: (a) malignant lesion was misclassified as benign; (b) benign lesion was misclassified as malignant.

For the single image-based model, the original EBUS images of 200 patients were augmented to obtain 602 images (305 images in the benign class and 297 images in the malignant class). Figure 4.13(b) depicts the confusion matrix of the single image-based model where three malignant lesions were misclassified as benign, and seven benign lesions were misclassified as malignant.

Figure 4.15 depicts the misclassification of the single image-based model. Figure 4.15(a) shows a malignant lesion that was misclassified as benign because the texture of the lesion was quite smooth, which is a common feature of benign lesion. Figure 4.15(b) shows a benign lesion that was misclassified as malignant because its texture is heterogeneous.

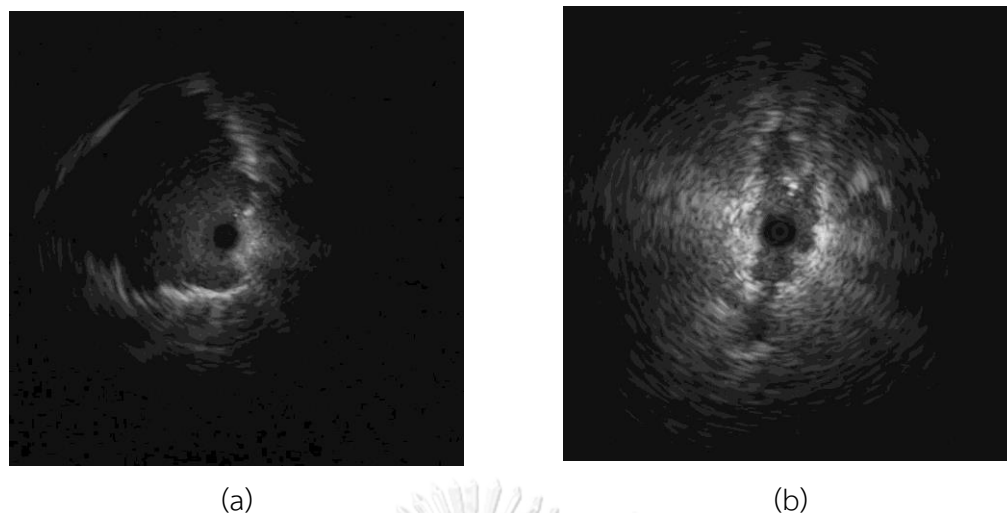


Figure 4.15 Misclassification of the single image-based model: (a) malignant lesion was misclassified as benign; (b) benign lesion was misclassified as malignant.

Next, the multi-patch-based model used the same image data of 200 patients that were used for the single image-based model, but each image was divided into patches. Depending on the region of lesion, the number of patches in each EBUS image can be from one to fourteen. After augmentation and WOI selection, 6,795 patches were obtained with 3,335 benign patches and 3,460 malignant patches. After the model was trained by 6,369 patches, each patch extracted from the test image was classified independently. The classification result of each image was determined from the results of all patches using the decision threshold. In this experiment, T was set to 0.63. It means that if the ratio of the number of malignant patches to the total number of patches is greater than 0.63, this EBUS image is classified as malignant; otherwise, it is classified as benign. The confusion matrix of the multi-patch-based model is depicted in Figure 4.13(c), which indicates that three malignant lesions were misclassified as benign, while two benign lesions were misclassified as malignant.

Figure 4.16 depicts the misclassification results of the multi-patch-based model. Figure 4.16(a) depicts a malignant lesion that was misclassified as benign, while Figure 4.16(b) depicts a benign lesion that was misclassified as malignant. The main reason for misclassification of Figure 4.16(a) is because the lesion region is too small, which

allows only a few patches to be used for classification; whereas the misclassification of Figure 4.16(b) is because the texture of the lesion is heterogeneous.

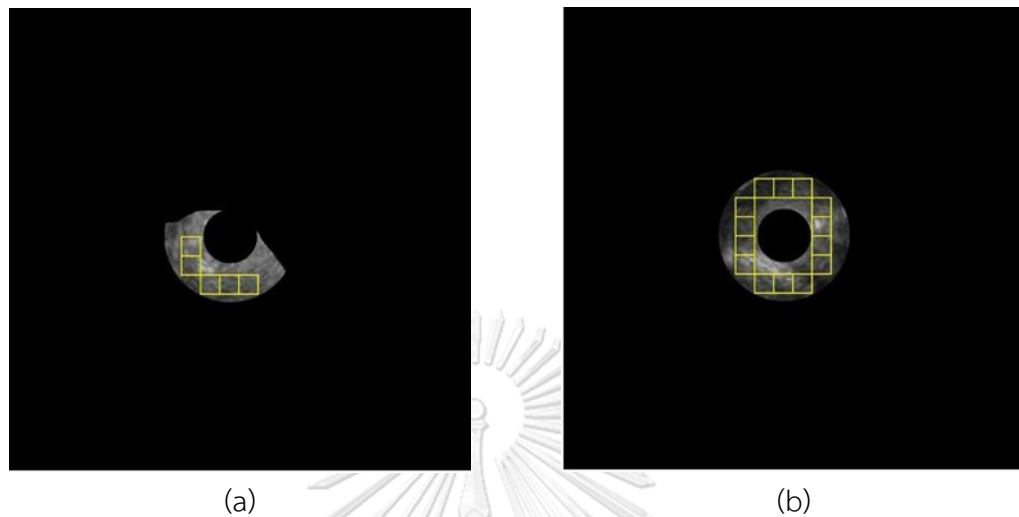


Figure 4.16 Misclassification of the multi-patch-based model: (a) malignant lesion was misclassified as benign; (b) benign lesion was misclassified as malignant.

From the statistical results in Table 4.6, it can be seen that the radiomics feature and patient data-based model and the multi-patch-based model yield high accuracy regardless of the number of image data; whereas the single image-based model yields the lowest accuracy. The main problem of the single image-based model is that CNN needs a very large dataset to obtain good results. However, the texture of the boundary and the surrounding areas of a lesion are also important features, thus this paper proposes to integrate the statistical results of the three models to perform the final classification using the weighted ensemble classification to assign the weight to each model based on the classification performance. In this paper, w_1 , w_2 , and w_3 were set to 0.41, 0.08, and 0.51, based on the performance of the models. The optimal cutoff was set to 0.53, which is defined by the value that yields the highest accuracy during the training. The lesions were divided into two classes: benign when $P(I) \leq 0.53$ and malignant when $P(I) > 0.53$. The proposed framework's confusion matrix is depicted in Figure 4.13(d), which indicates that all malignant lesions were correctly classified, while only two benign lesions were misclassified as malignant.

Figure 4.17 depicts the effectiveness of the proposed framework. Figure 4.17(a) shows the correct classification result of the proposed framework while two out of three classification results from three models are incorrect; i.e., the radiomics feature and patient data-based model and the single image-based model misclassified benign lesion as malignant. Figure 4.17(b) shows the correct classification result of the proposed framework, while two out of three classification results from three models are incorrect; i.e., the single image-based model and the multi-patch-based model misclassified the malignant lesion as benign.

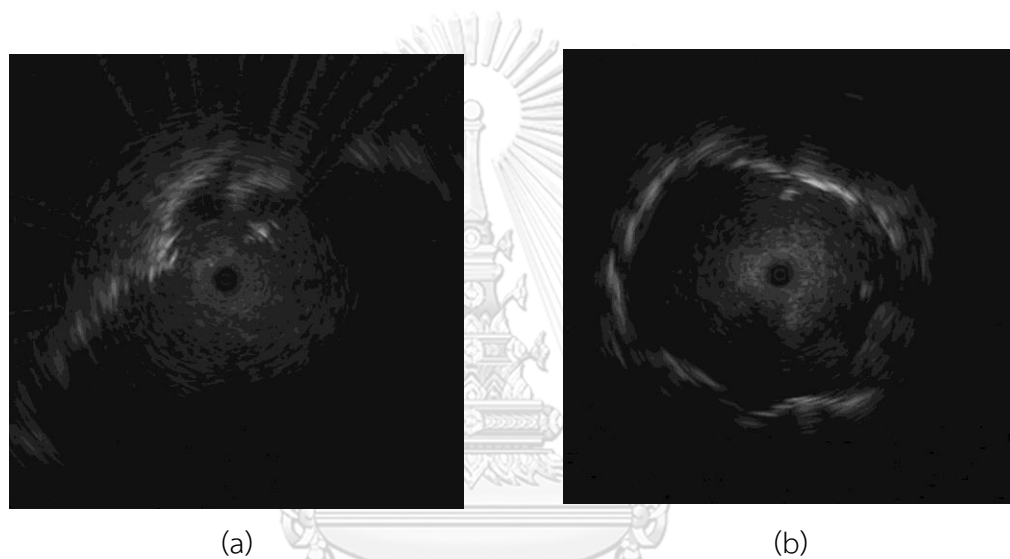


Figure 4.17 Two out of three models misclassified a lesion, but the proposed framework can classify correctly. (a) benign lesion was misclassified as malignant in radiomics feature and patient data-based model and multi-patch-based model. (b) benign lesion was misclassified as malignant in single image-based model and multi-patch-based model.

Table 4.6 displays the classification performance of all classification models. The proposed framework yields accuracy, sensitivity, specificity, positive predictive value, and a negative predictive value of 95.00, 100, 86.67, 92.59, and 100, respectively. Furthermore, by comparing the ROC curves and AUC values of all classification models in Figure 4.18, the AUC value obtained by using the proposed framework is 0.9333, which is higher than those of the other three models.

The proposed framework performs well, but it still has some limitations. First, there is no evidence that the proposed framework works well with other types of medical images. Second, the number of patches depends on the region of lesion in each image, thus a lesion with only a few patches can be easily misclassified in a multi-patch-based model.

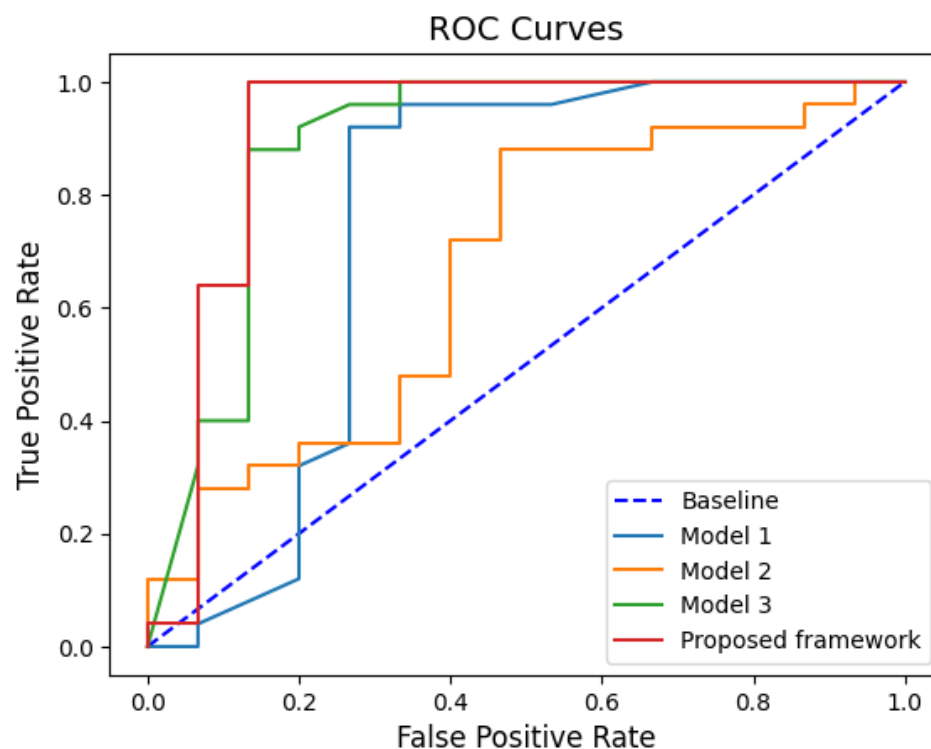


Figure 4.18 ROC curves and AUC values of the classification models.

4.5 Conclusions

In this paper, a novel pulmonary lesion classification framework for EBUS images was proposed by integrating three classification models with the weighted ensemble classification. The proposed framework works well with imbalanced data and small datasets. The radiomics feature and patient data-based model is suitable for any size of the dataset because it classifies a lesion based on both radiomics features and patient data that contain substantial amounts of relevant information, such as texture, shape, size, age, and gender. It also works well for an imbalanced

dataset. The single image-based model uses the global characteristics of a lesion from the entire EBUS images to train the model. Thus, the model can learn and extract the dominant features from an image by the model itself. However, the disadvantage of this model is that it needs a large volume of data to obtain good results. On the other hand, the multi-patch-based model uses local characteristics of a lesion from each patch. By integrating these three models with the weighted ensemble classification, the proposed framework can improve the classification results by using both local and global characteristics of a lesion. The proposed framework achieves promising pulmonary lesion classification results and outperforms individual models. Due to ethics concerns, data insufficiency is a common problem in medical applications, and the proposed framework can tackle this problem. In the future, the proposed framework will be tested on different sets of medical images.

Author Contributions: Conceptualization, B.K. and R.L.; methodology, B.K. and R.L.; software, B.K.; validation, B.K. and R.L.; formal analysis, B.K. and R.L.; investigation, B.K. and R.L.; writing—original draft preparation, B.K.; writing—review and editing, R.L.; visualization, B.K.; supervision, R.L.; project administration, R.L. All authors have read and agreed to the published version of the manuscript.

Funding: This research received no external funding.

Institutional Review Board Statement: Not applicable.

Informed Consent Statement: Not applicable.

Data Availability Statement: Not applicable.

Acknowledgments: The authors would like to thank Anan Wattanathum, M.D. and Jutamas Dechsanga, M.D. of Phramongkutklao Hospital in Bangkok, Thailand, for providing EBUS images and making recommendations about EBUS images. The authors would also like to thank the Development and Promotion of Science and Technology Talents Project for providing financial support throughout the doctoral program.

Conflicts of Interest: The authors declare no conflict of interest.

References

- [1] H. Sung *et al.*, "Global cancer statistics 2020: GLOBOCAN estimates of incidence and mortality worldwide for 36 cancers in 185 countries," *CA: a cancer journal for clinicians*, vol. 71, no. 3, pp. 209-249, 2021.
- [2] L. H. Araujo, L. Horn, R. E. Merritt, K. Shilo, M. Xu-Welliver, and D. P. Carbone, "Cancer of the lung: non-small cell lung cancer and small cell lung cancer," in *Abeloff's Clinical Oncology*: Elsevier, 2020, pp. 1108-1158. e16.
- [3] F. Islami *et al.*, "Proportion and number of cancer cases and deaths attributable to potentially modifiable risk factors in the United States," *CA: a cancer journal for clinicians*, vol. 68, no. 1, pp. 31-54, 2018.
- [4] M. Wang, R. S. Herbst, and C. Boshoff, "Toward personalized treatment approaches for non-small-cell lung cancer," *Nature medicine*, vol. 27, no. 8, pp. 1345-1356, 2021.
- [5] G. A. Silvestri *et al.*, "Methods for staging non-small cell lung cancer: diagnosis and management of lung cancer: American College of Chest Physicians evidence-based clinical practice guidelines," *Chest*, vol. 143, no. 5, pp. e211S-e250S, 2013.
- [6] L. T. Tanoue, N. T. Tanner, M. K. Gould, and G. A. Silvestri, "Lung cancer screening," *American journal of respiratory and critical care medicine*, vol. 191, no. 1, pp. 19-33, 2015.
- [7] B. Zaric *et al.*, "Advanced bronchoscopic techniques in diagnosis and staging of lung cancer," (in eng), *J Thorac Dis*, vol. 5 Suppl 4, no. Suppl 4, pp. S359-S370, 2013, doi: 10.3978/j.issn.2072-1439.2013.05.15.
- [8] K. Czarnecka-Kujawa and K. Yasufuku, "The role of endobronchial ultrasound versus mediastinoscopy for non-small cell lung cancer," (in eng), *J Thorac Dis*, vol. 9, no. Suppl 2, pp. S83-S97, 2017, doi: 10.21037/jtd.2017.03.102.
- [9] Q. Tian, L. A. Chen, R. T. Wang, Z. Yang, and Y. An, "The reasons of false negative results of endobronchial ultrasound-guided transbronchial needle aspiration in the diagnosis of intrapulmonary and mediastinal malignancy," *Thoracic Cancer*, vol. 4, no. 2, pp. 186-190, 2013.
- [10] N. Kurimoto, M. Murayama, S. Yoshioka, and T. Nishisaka, "Analysis of the internal structure of peripheral pulmonary lesions using endobronchial ultrasonography," (in English), *Chest*, vol. 122, no. 6, pp. 1887-1894, Dec 2002, doi: DOI 10.1378/chest.122.6.1887.
- [11] X. Zheng, L. Wang, J. Chen, F. Xie, Y. Jiang, and J. Sun, "Diagnostic value of radial endobronchial ultrasonographic features in predominant solid peripheral pulmonary lesions," (in eng), *J Thorac Dis*, vol. 12, no. 12, pp. 7656-7665, 2020, doi: 10.21037/jtd-2020-abpd-004.

- [12] T. Izumo, S. Sasada, C. Chavez, Y. Matsumoto, and T. Tsuchida, "Endobronchial ultrasound elastography in the diagnosis of mediastinal and hilar lymph nodes," *Japanese journal of clinical oncology*, vol. 44, no. 10, pp. 956-962, 2014.
- [13] M. Hernández Roca *et al.*, "Diagnostic value of elastography and endobronchial ultrasound in the study of hilar and mediastinal lymph nodes," *Journal of bronchology & interventional pulmonology*, vol. 26, no. 3, pp. 184-192, 2019.
- [14] X. Zhi, J. Chen, F. Xie, J. Sun, and F. J. Herth, "Diagnostic value of endobronchial ultrasound image features: A specialized review," *Endoscopic ultrasound*, vol. 10, no. 1, p. 3, 2021.
- [15] K. Morikawa, N. Kurimoto, T. Inoue, M. Mineshita, and T. Miyazawa, "Histogram-based quantitative evaluation of endobronchial ultrasonography images of peripheral pulmonary lesion," *Respiration*, vol. 89, no. 2, pp. 148-154, 2015.
- [16] I. O. Alici, N. Yılmaz Demirci, A. Yılmaz, J. Karakaya, and E. Özyaydın, "The sonographic features of malignant mediastinal lymph nodes and a proposal for an algorithmic approach for sampling during endobronchial ultrasound," *The clinical respiratory journal*, vol. 10, no. 5, pp. 606-613, 2016.
- [17] B. Khomkham and R. Lipikorn, "Pulmonary lesion classification from endobronchial ultrasonography images using adaptive weighted-sum of the upper and lower triangular gray-level co-occurrence matrix," *International Journal of Imaging Systems and Technology*, vol. 31, no. 3, pp. 1280-1293, 2021.
- [18] W. Gómez, W. C. A. Pereira, and A. F. C. Infantosi, "Analysis of co-occurrence texture statistics as a function of gray-level quantization for classifying breast ultrasound," *IEEE transactions on medical imaging*, vol. 31, no. 10, pp. 1889-1899, 2012.
- [19] A. D. Jia, B. Z. Li, and C. C. Zhang, "Detection of cervical cancer cells based on strong feature CNN-SVM network," *Neurocomputing*, vol. 411, pp. 112-127, 2020.
- [20] J. Tan *et al.*, "3D-GLCM CNN: A 3-Dimensional Gray-Level Co-Occurrence Matrix-Based CNN Model for Polyp Classification via CT Colonography," *IEEE transactions on medical imaging*, vol. 39, no. 6, pp. 2013-2024, 2019.
- [21] M. Z. Islam, M. M. Islam, and A. Asraf, "A combined deep CNN-LSTM network for the detection of novel coronavirus (COVID-19) using X-ray images," *Informatics in medicine unlocked*, vol. 20, p. 100412, 2020.
- [22] Y. Li, Z. Zhang, C. Dai, Q. Dong, and S. Badrigilan, "Accuracy of deep learning for automated detection of pneumonia using chest X-Ray images: A systematic review and meta-analysis," *Computers in Biology and Medicine*, p. 103898, 2020.
- [23] Q. Zhang *et al.*, "A GPU-based residual network for medical image classification in smart medicine," *Information Sciences*, vol. 536, pp. 91-100, 2020.

- [24] L. Cai, T. Long, Y. Dai, and Y. Huang, "Mask R-CNN-based detection and segmentation for pulmonary nodule 3D visualization diagnosis," *IEEE Access*, vol. 8, pp. 44400-44409, 2020.
- [25] Q. Wang, Y. Zheng, G. Yang, W. Jin, X. Chen, and Y. Yin, "Multiscale rotation-invariant convolutional neural networks for lung texture classification," *IEEE journal of biomedical and health informatics*, vol. 22, no. 1, pp. 184-195, 2017.
- [26] M. Anthimopoulos, S. Christodoulidis, L. Ebner, A. Christe, and S. Mougiakakou, "Lung pattern classification for interstitial lung diseases using a deep convolutional neural network," *IEEE transactions on medical imaging*, vol. 35, no. 5, pp. 1207-1216, 2016.
- [27] C.-H. Chen *et al.*, "Computer-aided diagnosis of endobronchial ultrasound images using convolutional neural network," *Computer methods and programs in biomedicine*, vol. 177, pp. 175-182, 2019.
- [28] Y. Lei, J. Zhang, and H. Shan, "Strided Self-Supervised Low-Dose CT Denoising for Lung Nodule Classification," *Phenomics*, vol. 1, no. 6, pp. 257-268, 2021.
- [29] Y. Lei, Y. Tian, H. Shan, J. Zhang, G. Wang, and M. K. Kalra, "Shape and margin-aware lung nodule classification in low-dose CT images via soft activation mapping," *Medical image analysis*, vol. 60, p. 101628, 2020.
- [30] X. Guo *et al.*, "An ensemble learning method based on ordinal regression for COVID-19 diagnosis from chest CT," *Physics in Medicine & Biology*, vol. 66, no. 24, p. 244001, 2021.
- [31] N. Salem, H. Malik, and A. Shams, "Medical image enhancement based on histogram algorithms," *Procedia Computer Science*, vol. 163, pp. 300-311, 2019.
- [32] P. Janani, J. Premalatha, and K. Ravichandran, "Image enhancement techniques: A study," *Indian Journal of Science and Technology*, vol. 8, no. 22, pp. 1-12, 2015.
- [33] C.-C. Yang, "Image enhancement by modified contrast-stretching manipulation," *Optics & Laser Technology*, vol. 38, no. 3, pp. 196-201, 2006/04/01/ 2006, doi: <https://doi.org/10.1016/j.optlastec.2004.11.009>.
- [34] V. Chalana and Y. Kim, "A methodology for evaluation of boundary detection algorithms on medical images," *IEEE Transactions on medical imaging*, vol. 16, no. 5, pp. 642-652, 1997.
- [35] N. K. Tomar *et al.*, "Fanet: A feedback attention network for improved biomedical image segmentation," *arXiv preprint arXiv:2103.17235*, 2021.
- [36] D. Jha *et al.*, "Real-time polyp detection, localization and segmentation in colonoscopy using deep learning," *IEEE Access*, vol. 9, pp. 40496-40510, 2021.
- [37] W. Suraworachet, R. Lipikorn, and A. Wattanatham, "Pulmonary lesion boundary detection from an endobronchial ultrasonogram using polar sector maximum intensity," *Int. J. Electron. Electr. Eng.*, vol. 4, no. 2, pp. 185-188, 2016.

- [38] J. J. Van Griethuysen *et al.*, "Computational radiomics system to decode the radiographic phenotype," *Cancer research*, vol. 77, no. 21, pp. e104-e107, 2017.
- [39] F. S. Roque *et al.*, "Using electronic patient records to discover disease correlations and stratify patient cohorts," *PLoS computational biology*, vol. 7, no. 8, p. e1002141, 2011.
- [40] B. C. Ross, "Mutual information between discrete and continuous data sets," *PloS one*, vol. 9, no. 2, p. e87357, 2014.
- [41] A. T. Azar, H. I. Elshazly, A. E. Hassanien, and A. M. Elkorany, "A random forest classifier for lymph diseases," *Computer methods and programs in biomedicine*, vol. 113, no. 2, pp. 465-473, 2014.
- [42] S.-H. Wang and Y.-D. Zhang, "DenseNet-201-based deep neural network with composite learning factor and precomputation for multiple sclerosis classification," *ACM Transactions on Multimedia Computing, Communications, and Applications (TOMM)*, vol. 16, no. 2s, pp. 1-19, 2020.
- [43] T. Shermin, S. W. Teng, M. Murshed, G. Lu, F. Sohel, and M. Paul, "Enhanced transfer learning with imagenet trained classification layer," in *Pacific-Rim Symposium on Image and Video Technology*, 2019: Springer, pp. 142-155.
- [44] A. Krizhevsky, I. Sutskever, and G. E. Hinton, "Imagenet classification with deep convolutional neural networks," *Advances in neural information processing systems*, vol. 25, 2012.
- [45] D. Jimenez, "Dynamically weighted ensemble neural networks for classification," in *1998 IEEE International Joint Conference on Neural Networks Proceedings. IEEE World Congress on Computational Intelligence (Cat. No.98CH36227)*, 4-9 May 1998 1998, vol. 1, pp. 753-756 vol.1, doi: 10.1109/IJCNN.1998.682375.

CHAPTER 5

DISCUSSIONS AND CONCLUSIONS

This chapter concludes and discusses the dissertation. The first section summarizes the main research findings and the contributions of this dissertation, followed by a discussion on the limitations and potential future research related to this dissertation.

5.1 Discussions and Conclusions

From the experimental results on the proposed features in Article 1 called AWSL and AWSU, together with a method for pulmonary lesion classification using a GA with SVM. The proposed features are suitable for representing heterogeneity characteristics because they determine the differences between intensities by discarding the similarities of the elements along the diagonal line of GLCM. By combining the proposed features with standard features, the performance of all classifiers can be improved. Furthermore, by using GA to select only features relevant to pulmonary lesion classification, the performance of the classifiers could be improved even further. The classification results show that using more features does not guarantee better performance; instead, it is critical to use only the relevant features. As a result, the proposed method for pulmonary lesion classification is robust, especially for small datasets.

From the experimental results for the proposed model in Article 2, a novel pulmonary lesion classification framework for EBUS images is proposed by integrating three classification models with the weighted ensemble classification. The proposed framework works well with imbalanced data and small datasets. The radiomics feature and patient data-based model are suitable for any size of the dataset because it classifies a lesion based on both radiomics features and patient data that contain lots of relevant information, such as texture, shape, size, age, and gender. It also works well for an imbalanced dataset. The single image-based model uses the global characteristics of a lesion from the entire EBUS images to train the model. Thus, the

model can learn and extract the dominant features from an image by the model itself. However, the disadvantage of this model is that it needs a large volume of data to obtain good results. On the contrary, the multi-patch-based model uses local characteristics of a lesion from each patch. These local characteristics focus on the patterns of texture. By integrating these three models with the weighted ensemble classification, the proposed framework can improve the classification results by using both local and global characteristics of a lesion. The proposed framework achieves promising pulmonary lesion classification results and outperforms individual models.

Comparing the performance of Article 1 and 2, the performance of the proposed features in Article 1 achieves 86.52 percent accuracy, 87.27 percent sensitivity, 85.29 percent specificity, 90.57 percent positive predictive value, 80.56 percent negative predictive value, and 0.8628 area under the curve. The proposed model in Article 2 achieves 95.00 percent accuracy, 100.00 percent sensitivity, 86.67 percent specificity, 92.59 percent positive predictive value, 100.00 percent negative predictive value, and 0.9333 percent area under the curve. Article 1 input data consists only of EBUS images, whereas Article 2 input data combines both EBUS images and patient data. Although extracting features from EBUS images using the handcrafted features relevant to medical knowledge in Article 1 achieves acceptable accuracy, classification performance can be improved further by combining these features with the pulmonary lesion classification framework in Article 2.

In the radiomics feature and patient data-based model of the proposed framework, 57 out of 89 features are selected with the criteria that use MI scores greater than zero. The performance of the radiomics feature and patient data-based model for various MI scores is shown in Figure 5.1. From the comparison, the optimal threshold value that yields the highest accuracy for this dataset is zero.

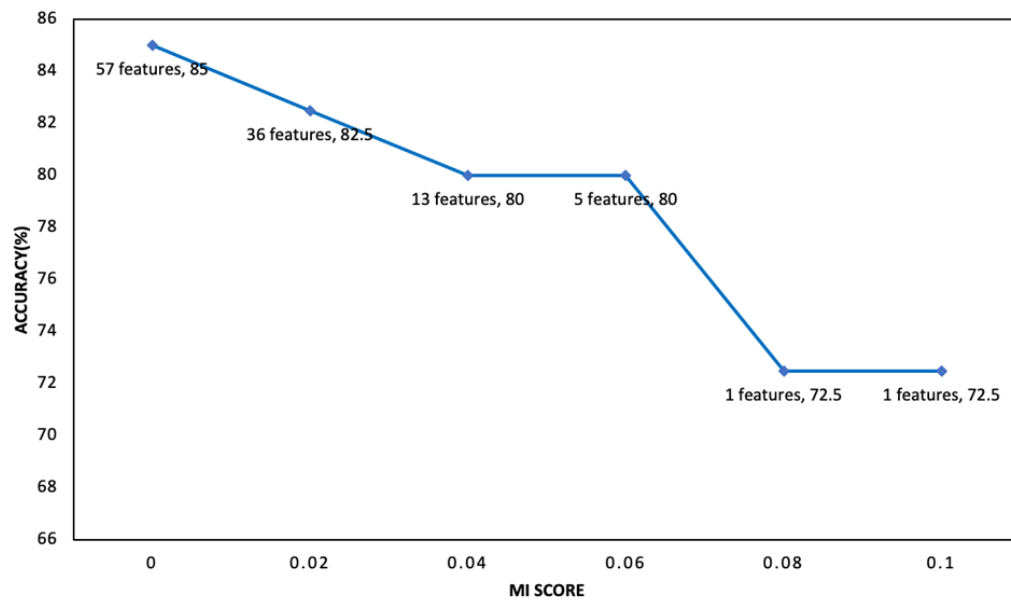


Figure 5.1 Comparison graph of MI scores for the radiomics feature and patient data-based model.

For performance evaluation, other augmentations, such as adding noise and blurring, were applied to the test set. The test EBUS images were augmented by adding speckle noise, gaussian noise, salt and paper noise, and motion blur to generate other 160 test data as shown in Table 5.1. Examples of augmented test EBUS images are shown in Figure 5.2.

Table 5.1 Distribution of test EBUS image data after applying augmentation.

	Malignant	Benign	All
Original EBUS image data	25	15	40
Augmented image data	100	60	160
Total of test image data	125	75	200

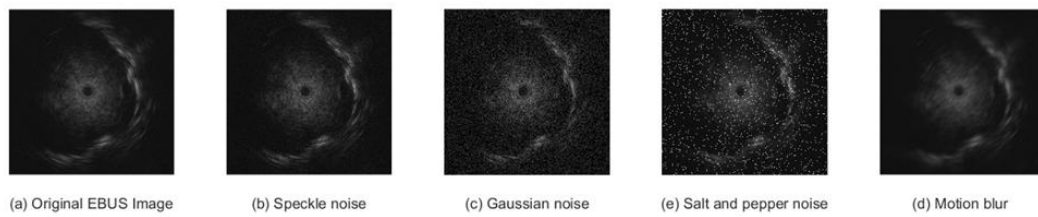


Figure 5.2 Examples of augmented test EBUS image data.

After executing the proposed framework with augmented test image data, the statistical results are shown in Table 5.2. The performance of the proposed framework achieves 78.5 percent accuracy, 97.6 percent sensitivity, 46.67 percent specificity, 75.30 percent positive predictive value, and 92.10 percent negative predictive value. The statistical results reveal that the proposed framework outperforms individual models. The confusion matrices obtained after executing the proposed framework with augmented test image data are shown in Figure 5.3.

Table 5.2 The classification performance of different classification models.

	Acc	Sen	Spec	PPV	NPV
Radiomics feature and patient data-based model	71.50	84.80	49.33	73.61	66.07
Single image-based model	68.00	91.20	29.33	68.26	66.67
Multi-patch-based model	73.00	95.20	36.00	71.26	81.82
Proposed framework	78.50	97.60	46.67	75.31	92.11

The values in bold font indicate the best index values.

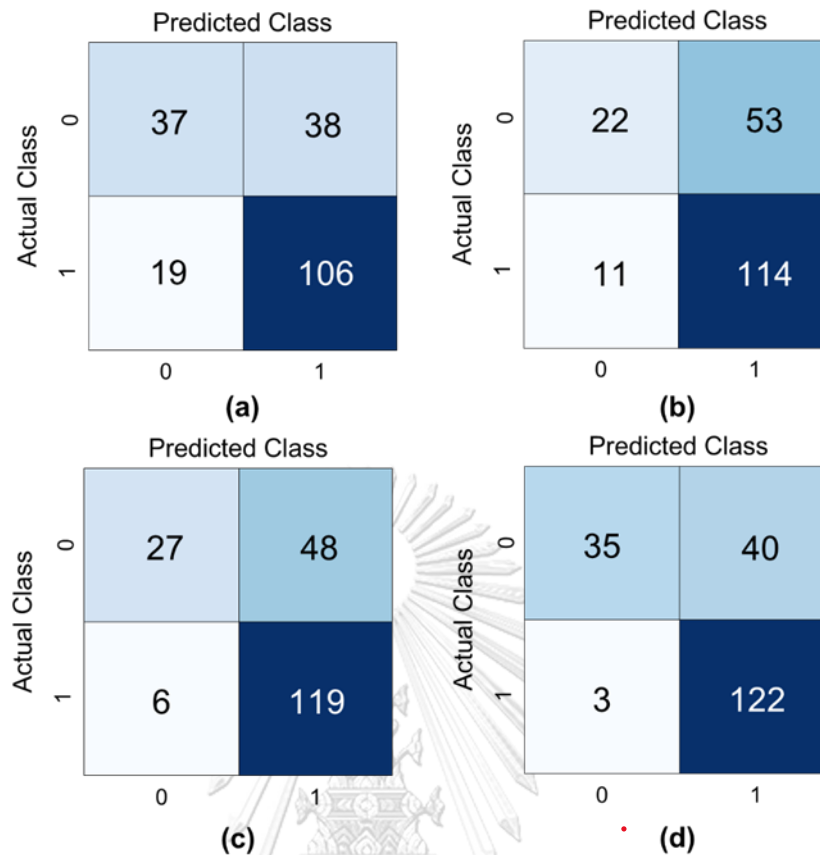


Figure 5.3 The confusion matrices of the proposed framework with augmented test data:(a) the radiomics feature and patient data-based model; (b) the single image-based model; (c) the multi-patch-based model, and (d) the proposed framework.

5.2 Limitations of Work

The proposed framework still has some limitations. There is no evidence that the proposed framework works well with other types of medical images, and the number of patches for each EBUS image depends on the region of a lesion; therefore, a lesion with only a few patches can be easily misclassified in a multi-patch-based model. The accuracy of the single image-based model is the lowest because the number of input data is small, thus the model does not have enough information to learn all patterns to yield high classification performance.

5.3 Suggestions and Future Works

For future work, the classification accuracy can be improved further by developing new features which can capture other important characteristics of malignancy such as continuous margin, hyperechoic dot or arc, luminant area, and anechoic area, and modifying the DL architecture to make it more suitable for EBUS images. Moreover, the segmentation of pulmonary lesions might be addressed by unsupervised approaches due to the small sample size of the analyzed dataset. The proposed framework will be tested on different sets of medical images. Furthermore, the time complexity of the proposed framework will be considered in the subsequent work.



APPENDIX

The algorithm for calculating the parameters of the weighted ensemble classification

The parameters of the weighted ensemble classification used in this dissertation were obtained from the algorithm below. The input parameters consist of the statistical results of radiomics feature and patient data-based model; P_1 , the single image-based model; P_2 , the multi-patch-based model; P_3 , and the actual values, Tar . The purpose of the algorithm is to find the weights of the models and the cutoff value that yield the highest accuracy during the training phase. These parameters were then applied in the test phase. In the first step of the algorithm, the initial cutoff value and the accuracy were set to zero, and the weights of the models were set to the values from zero to one which yielded the weight sums of the models equal to one. In the second step, the prediction value of the weighted ensemble classification; P was calculated by summation of the multiplication of the statistical results of the models and their weights. In the final step, the algorithm searched for the parameters with the highest accuracy. The algorithm returns the accuracy; Acc , the cutoff value; c , the weight of the radiomics feature and patient data-based model; w_1 , the weight of the single image-based model; w_2 , and the weight of the multi-patch-based model; w_3 .

Input: The list of statistical results of each Model, P_1, P_2, P_3 ; list of actual values, Tar

Output: Accuracy, Acc ; the weight of each model, w_1, w_2, w_3 ; cutoff value, c

Initialize indices

$c = 0$; $Acc = 0$; list of weight w_1 , $Lw_1 = [0, 0.01, 0.02, \dots, 1]$; list of weight w_2 , $Lw_2 = [0, 0.01, 0.02, \dots, 1]$

for i in Lw_1 **then**

for j in Lw_2 **then**

$$k = 1 - i - j$$

$$P = i \times P_1 + j \times P_2 + k \times P_3$$

$Temp_acc, Temp_c = \text{find_weight_acc_max}(P, Tar)$

if $Acc < Temp_acc$ **then**

$Acc = Temp_acc$; $c = Temp_c$;

$w_1 = i$; $w_2 = j$; $w_3 = k$;

endif จุฬาลงกรณ์มหาวิทยาลัย

endfor CHULALONGKORN UNIVERSITY

 Remove j from Lw_2

endfor

return Acc, w_1, w_2, w_3, c

Algorithm: find_weight_acc_max

Input: list of prediction values, P ; list of actual values, Tar

Output: Accuracy, Acc , Threshold value, T

Initialize indices

$T = 0$; $Acc = 0$; $W = list()$;

for i in 0 to 1 increase by 0.01 **then**

$L = cutoff(i, P)$

$temp = measure_performance(L, Tar)$

Append $temp$ to W

if $Acc < temp$ **then**

$Acc = temp$; $T = i$;

endif

endfor

return Acc, T

Algorithm: cutoff

Input: list of prediction values, P ; cutoff value, c

Output: list of labeled class values, L

Initialize indices

$L = list()$;

for j in P **then**

if $j > c$ **then**

$l = 1$

else

$l = 0$

endif

 Append l to L

endfor

return L



จุฬาลงกรณ์มหาวิทยาลัย

CHULALONGKORN UNIVERSITY

Algorithm: measure_performance

Input: list of prediction values, P ; list of actual values, Tar

Output: Accuracy, Acc

Initialize indices

$nCtr = 0$; $Acc = 0$

for i in range(len(P)) **then**

if $P[i]=Tar[i]$ **then**

$nCtr = nCtr+1$

endif

endfor

$Acc = nCtr*100/ \text{len}(P)$

return Acc

REFERENCES

- [1] H. Sung *et al.*, "Global cancer statistics 2020: GLOBOCAN estimates of incidence and mortality worldwide for 36 cancers in 185 countries," *CA: a cancer journal for clinicians*, vol. 71, no. 3, pp. 209-249, 2021.
- [2] R. L. Siegel, K. D. Miller, H. E. Fuchs, and A. Jemal, "Cancer statistics, 2022," *CA: a cancer journal for clinicians*, 2022.
- [3] T. Reungwetwattana, S. Oranratnachai, P. Puataweepong, V. Tangsujaritvijit, and P. Chermtanomwong, "Lung cancer in Thailand," *Journal of Thoracic Oncology*, vol. 15, no. 11, pp. 1714-1721, 2020.
- [4] N. Howlader *et al.*, "SEER cancer statistics review, 1975–2018," *National Cancer Institute*, 2021.
- [5] J. M. Pacheco *et al.*, "Natural history and factors associated with overall survival in stage IV ALK-rearranged non–small cell lung cancer," *Journal of Thoracic Oncology*, vol. 14, no. 4, pp. 691-700, 2019.
- [6] D. E. Wood *et al.*, "Lung cancer screening, version 3.2018, NCCN clinical practice guidelines in oncology," *Journal of the National Comprehensive Cancer Network*, vol. 16, no. 4, pp. 412-441, 2018.
- [7] W. E. Zahnd and J. M. Eberth, "Lung cancer screening utilization: a behavioral risk factor surveillance system analysis," *American journal of preventive medicine*, vol. 57, no. 2, pp. 250-255, 2019.
- [8] T. Kramer and J. T. Annema, "Advanced bronchoscopic techniques for the diagnosis and treatment of peripheral lung cancer," *Lung Cancer*, vol. 161, pp. 152-162, 2021.
- [9] S. Jiang, F. Xie, X. Mao, H. Ma, and J. Sun, "The value of navigation bronchoscopy in the diagnosis of peripheral pulmonary lesions: a meta-analysis," *Thoracic Cancer*, vol. 11, no. 5, pp. 1191-1201, 2020.
- [10] J. Xiang, H. Yan, J. Li, X. Wang, H. Chen, and X. Zheng, "Transperineal versus transrectal prostate biopsy in the diagnosis of prostate cancer: a systematic review and meta-analysis," *World journal of surgical oncology*, vol. 17, no. 1, pp. 1-11, 2019.
- [11] T. Gahlot, U. Parakh, K. Verma, B. Bhalotra, and N. Jain, "Endobronchial ultrasound-guided transbronchial needle aspiration in diagnosing mediastinal lymphadenopathy," (in eng), *Lung India*, vol. 34, no. 3, pp. 241-246, May-Jun 2017, doi: 10.4103/0970-2113.205339.
- [12] G. A. Silvestri *et al.*, "Methods for staging non-small cell lung cancer: diagnosis and management of lung cancer: American College of Chest Physicians evidence-based clinical practice guidelines," *Chest*, vol. 143, no. 5, pp. e211S-e250S, 2013.
- [13] M. Gomez and G. A. Silvestri, "Endobronchial ultrasound for the diagnosis and staging of lung cancer," *Proceedings of the American Thoracic Society*, vol. 6, no. 2, pp. 180-186, 2009.
- [14] X. Zheng, L. Wang, J. Chen, F. Xie, Y. Jiang, and J. Sun, "Diagnostic value of radial endobronchial ultrasonographic features in predominant solid peripheral pulmonary lesions," *J Thorac Dis*, vol. 12, no. 12, p. 7656, 2020.



จุฬาลงกรณ์มหาวิทยาลัย
CHULALONGKORN UNIVERSITY

VITA

NAME Banphatree Khomkham

DATE OF BIRTH 27 March 1992

PLACE OF BIRTH Bangkok

INSTITUTIONS ATTENDED Chulalongkorn University, Bangkok, TH July 2018
Master of Science: Applied Mathematics and
Computational Science

Khon Kaen University, Khon Kaen, TH March 2014
Bachelor of Science: Mathematics (First class honor)

PUBLICATION Khomkham, B., Wattanathum, A., & Lipikorn, R. (2017, October). Peripheral pulmonary lesion classification from endobronchial ultrasonography images using weight-sum of upper and lower GLCM feature. In 2017 7th IEEE International Conference on System Engineering and Technology (ICSET) (pp. 157-161). IEEE.

Dechsanga, J., Wattanathum, A., Wongsrichanalai, V., Promthong, K., Khomkham, B., Lipikorn, R., & Suravorachet, W. (2018). Predicted malignancy of pulmonary lesion by using tumor inspector version 1 program in Phramongkutklao Hospital. Journal of Southeast Asian Medical Research, 2(1), 37-44.

Khomkham, B., & Lipikorn, R. (2021). Pulmonary lesion classification from endobronchial ultrasonography images using adaptive weighted-sum of the upper and lower triangular gray-level co-occurrence matrix. International

Journal of Imaging Systems and Technology, 31(3), 1280-1293.

Khomkham, B., & Lipikorn, R. (2022). Pulmonary Lesion Classification Framework Using the Weighted Ensemble Classification with Random Forest and CNN Models for EBUS Images. *Diagnostics*, 12(7), 1552.

